

Density Functional Theory Techniques for Electron Energy Loss Analysis of Lithium Materials

Quentin Stoyel, Mining and Materials Engineering, McGill University,
Montreal

August 2018

A thesis submitted to McGill University in partial fulfillment of the requirements of the
degree of Masters of Science



©Quentin Stoyel 2018

Contents

Abstract	iii
Abrégé	iv
Acknowledgements	v
1 Introduction	1
2 Literature Review	4
2.1 Electron Energy Loss Spectroscopy	4
2.1.1 Electron Microscopy	4
2.1.2 EELS in Experiment	10
2.1.3 Lithium in EELS	13
2.1.4 Preprocessing	14
2.1.5 Other Experimental Techniques	18
2.2 Density Functional Theory (DFT)	19
2.2.1 DFT Background	19
2.2.2 Formulation	19
2.2.3 WIEN2k	25
2.2.4 Quantum Theory of Atoms in Molecules	26
2.2.5 Lithium in DFT	27
2.3 EELS Calculations	28
2.3.1 Time Dependent Density Functional Theory -TDDFT	29
2.3.2 Cross Section Approach	30

2.3.3	Beth Salpeter Equations -BSE	31
2.3.4	Core Hole Approximation	32
3	Methods	35
3.1	Improvement to Core Hole Shielding Calculations	35
3.2	Implementation	38
3.3	Calculation and Experimental Details	38
4	Results and Discussion	39
4.1	Lithium Oxide	39
4.2	Metallic Lithium	41
4.3	LiF	43
4.4	Li-LiF Mixture	44
4.5	Discussion	45
5	Conclusion	48
A	Calculation Details	50
A.1	Crystal Structures	50
A.2	DFT Parameters	51

Abstract

A new method of calculating the magnitude of the core hole screening in the case of lithium materials is developed and implemented for the accurate simulation of Energy Loss Near Edge Structure (ELNES). The method is used to verify the validity of performing electron energy loss spectroscopy at 30 keV to reduce beam damage. ELNES are calculated for metallic lithium, Li_2O , and LiF and marked improvements in agreement between calculation and experiment are observed. Superior quantitative and predictive abilities are also obtained with the new method. The technique uses linear response theory to relate the electron density and the core hole shielding contribution. This contribution is then implemented via a non integer core hole in final state rule density functional theory calculations.

Abrégé

Une nouvelle technique pour calculée l'intensité de masquage des trous d'etas de cœur est crée pour effectuer des simulations précises de la spectroscopie de perte d'énergie des électrons (spectroscopie EELS) des matireiux lithium. La methode est appliquée pour verifier la validité de conduire la spectroscopie EELS à 30 keV pour minimizer les dommages de la faisceau d'électron. Des spectres EELS sont calculées pour Li_2O , LiF et le lithium metalique et une meilleur accordance avec les resultats expérimentals est reconnue pour tous les matérieux. Des meillures caractéristiques quantitatives et prédictives sont aussi obtenues. La technique est bassée sur la théorie de la réponse linéaire et rélie la densité des électrons aux effets de masquage. Ces effets sont par la suite représentés avec une trou non-entière dans des calculations théorie de la fonctionnelle de la densité.

Acknowledgements

Many people need acknowledgement for helping make this work possible. Foremost amongst these are my supervisors, Professor Raynald Gauvin and Professor George P. Demopoulos for all their support, guidance, and valuable discussions. Equally essential to this work are Frédéric Voisard and Nicolas Brodusch who provided all the experimental results needed to verify the theoretical ones presented here. I would also like to thank Motoki Nakamura for taking the time to read and help edit my work and Frédéric Voisard for assistance in writing the French abstract. Acknowledgement is also due to the agencies who helped fund this work: NSERC and IREQ.

Support can come from a multitude of places in ways that are not always appreciated in the moment. To this end, I would like to thank everyone who helped instill me with love and excitement for physics and science. Whether it was in a classroom, a pub, or wandering the streets, those uttering the phrase “Hey, that’s an interesting problem,” inspired me into making this work happen. Finally, I would like to thank my parents for knowing that this was my path well before I did, and supporting me every step of the way.

Chapter 1

Introduction

The study of lithium materials has become increasingly relevant in recent years [1]. In particular, the field has been driven by the need to develop improved and more cost effective battery materials [1]. This drive has come from increasing demands for electric vehicles and portable electrical devices demanding longer lifetimes and faster charging. All aspects of lithium ion batteries can currently being improved as the theoretical limits have not yet been achieved in areas including capacity, charge density, and charge/discharge rates.

The theoretical limits in the case of lithium ion batteries are especially high, as lithium offers a range of advantages relative to other charge carriers. As the third element on the periodic table, lithium is extremely lightweight, allowing lithium ion batteries to be smaller and lighter without sacrificing lifetime. Lithium's small ion size makes it highly mobile, which leads to superior discharge rates. Furthermore, as an alkali earth metal with a single weakly bound valence electron, lithium is highly electropositive. As a result, lithium ion batteries can achieve higher operating voltages than alternatives such as nickle-cadmium or lead-acid batteries [2]. These comparative performance advantages to these alternatives are illustrated in Fig 1.1 [2].

The pursuit of further improving the performance of lithium batteries has shifted analysis

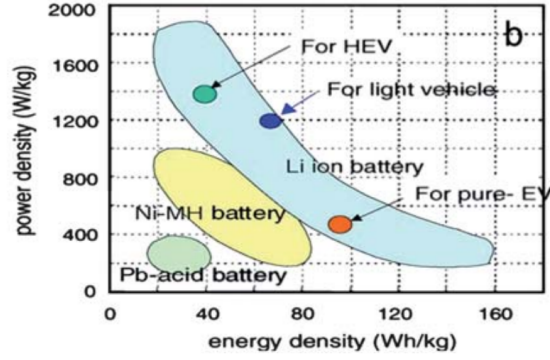


Figure 1.1: Plot illustrating the the power and energy densities achievable by three types of battery, as well as the minimum requirements for various types of electric vehicle, including hybrid electric vehicles (HEV), plug in hybrids (light vehicle). From Etacheri, 2011 [2].

of these materials increasingly towards measuring microstructure properties [3–5]. Identifying microscale features such as crystal structure, diffusion mechanics, and composition is an essential component of characterizing new battery materials [6]. These features are being increasingly analyzed through electron microscopy, due to high spatial resolution and increasing accessibility [7–9].

Lithium materials however, present a range of challenges to electron microscopy. Battery materials are becoming increasingly intricate and lithium’s light weight and ionizable nature make it particularly sensitive to electron beams [10]. These properties limit analysis largely to low dosage techniques to avoid damaging the samples long enough to acquire results. One such technique that is targeted for light elements such as lithium is electron energy loss spectroscopy (EELS) [11]. However, even using low dosage techniques, beam damage remains problematic for lithium materials and only with recent developments such as low voltage EELS, has lithium analysis become more routine [12]. As these new experimental techniques produce unprecedented results, a degree of theoretical support is required to confirm the methods and explain any irregularities.

Theoretical support for EELS comes most predominantly from methods based in density

functional theory (DFT). As in experiment, lithium’s lightweight nature complicates DFT calculations and results have been limited to qualitative findings [13; 14]. Much of the challenge in simulating EELS for lithium lies in the treatment of the electron hole created in excited atoms. Lithium’s few electrons mean that effects from the hole will almost always be present in the spectra and current methods in literature lack the subtlety to treat these effects.

The goal of this work is to calculate meaningful EELS spectra of lithium materials, specifically in the unprecedented context of EELS at 30 keV. This is accomplished by improving the treatment of core electron holes of lithium in DFT simulations.

The outline of this thesis is as follows: in Chapter 2 presents an overview of EELS, DFT and theoretical EELS calculations. Chapter 3 describes the improved method developed in this work, and Chapter 4 applies the method to a number of lithium materials. Chapter 5 concludes the results and addresses future work.

Chapter 2

Literature Review

The focus of this work lies in first principle theoretical calculations of EELS calculations, designed to be performed without experimental input. However, new theoretical techniques must be validated through comparison to experiment. To this end, this chapter presents an overview of experimental electron microscopy and energy loss spectroscopy (EELS) before discussing the basis of first principles calculations. The chapter concludes with a review of the various methods used to calculate EELS theoretically. The particularities of lithium materials are discussed at each step of this process.

2.1 Electron Energy Loss Spectroscopy

2.1.1 Electron Microscopy

The drive to improve increasingly refined battery materials relies on characterizing the nano scale features which define their properties [15]. At these length scales, even state of the art light microscopes lack the resolution to discern these features [16]. This limitation is due to the fact that nano scale features fall well below the diffraction limit of light microscopes, given by [17]:

$$d = \frac{\lambda}{2n \sin(\theta)} \tag{2.1}$$

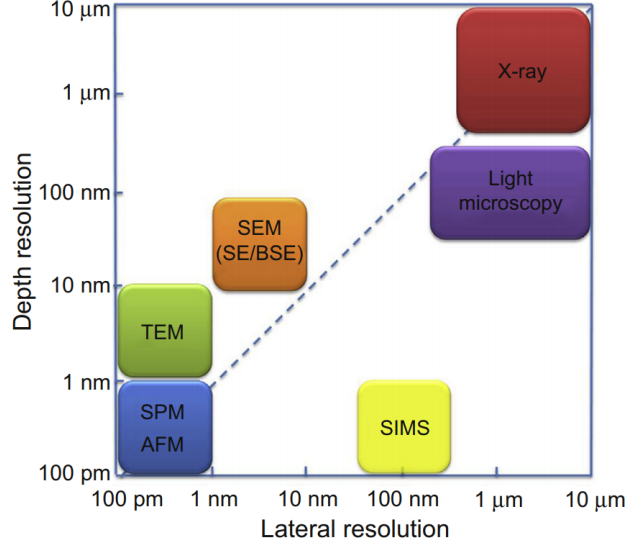


Figure 2.1: Resolution achievable by various techniques including Transmission and Scanning electron microscopy (TEM/SEM) and light microscopy, on a log-log scale. Taken from Inkson, 2016 [8]

Where n is the refractive index and d is the smallest distance between two discernible objects. For optical light ($\lambda = 400\text{-}800\text{nm}$), it is impossible to routinely achieve the desired resolution ($\sim 1\text{-}50\text{ nm}$) for characterization [16]. Electrons however, have a wavelength dictated by [15]:

$$\lambda = \frac{h}{\sqrt{2m_0eE}} \quad (2.2)$$

Where h is planck's constant, m_0 , e and E are the rest mass, charge and energy of an electron. In an electron microscope, electrons are accelerated to energies in the order of 1-100 keV giving them wavelengths in the range from 1-100 pm ($1\text{pm} = 10^{-12}\text{m}$), far smaller than the distances between atoms ($\sim 0.5\text{ nm}$) [18]. Electron microscopes can therefore achieve a far lower theoretical diffraction limit and are in fact currently limited by the technological constraints of the electron lenses [15]. This high resolution has made electron microscopy a key part of investigating material microstructure and is compared to other methods in Fig 2.1 [8].

In order to obtain images using electrons, electron microscopes use magnetic lenses to

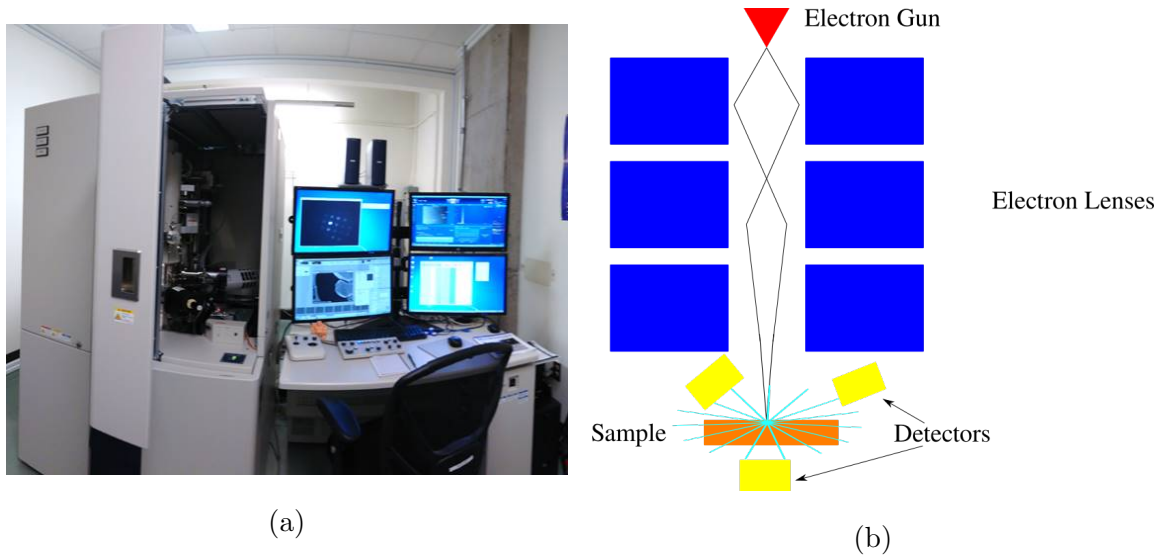


Figure 2.2: Example of an electron microscope (a) and working principles behind data acquisition (b).

focus a beam of high energy electrons onto a sample, and collect the assorted types of signals resulting from the interaction, see Fig 2.2.

The large number of different signals generated when the electron beam interacts with a sample, (depicted in Fig 2.3), can be used to perform a multitude of types of analysis [19]. A full discussion of the analysis methods at the disposal of electron microscopes is beyond the scope of this work and has been well documented elsewhere [11; 15; 19; 20]. Instead, this discussion is limited to electron energy loss spectroscopy (EELS). EELS is an electron microscopy technique that analyzes the transmitted inelastically scattered electrons, Fig 2.3[11]. It is mainly an analytic technique, however it is also possible to perform imaging with EELS [21]. EELS consists of collecting electrons that have passed entirely through the sample and binning them according to how much energy each one has lost, resulting in a spectrum such as shown in Fig 2.4. The numerous distinct features arise from the various mechanisms through which beam electrons can lose energy in the sample. Each mechanism results in a particular feature in the spectrum, of which the main ones are described below:

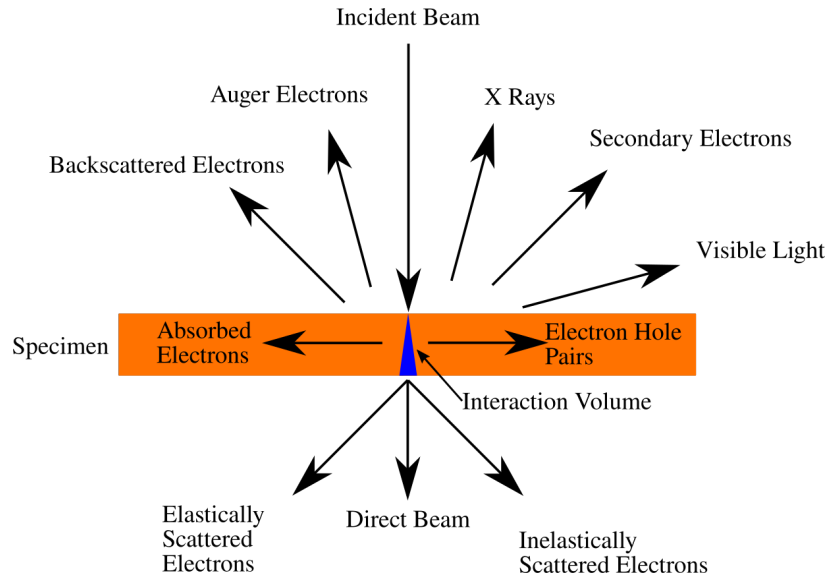


Figure 2.3: The numerous types of signals emitted when an electron beam encounters a sample in an electron microscope. Redrawn from Williams and Carter 2008 [19].

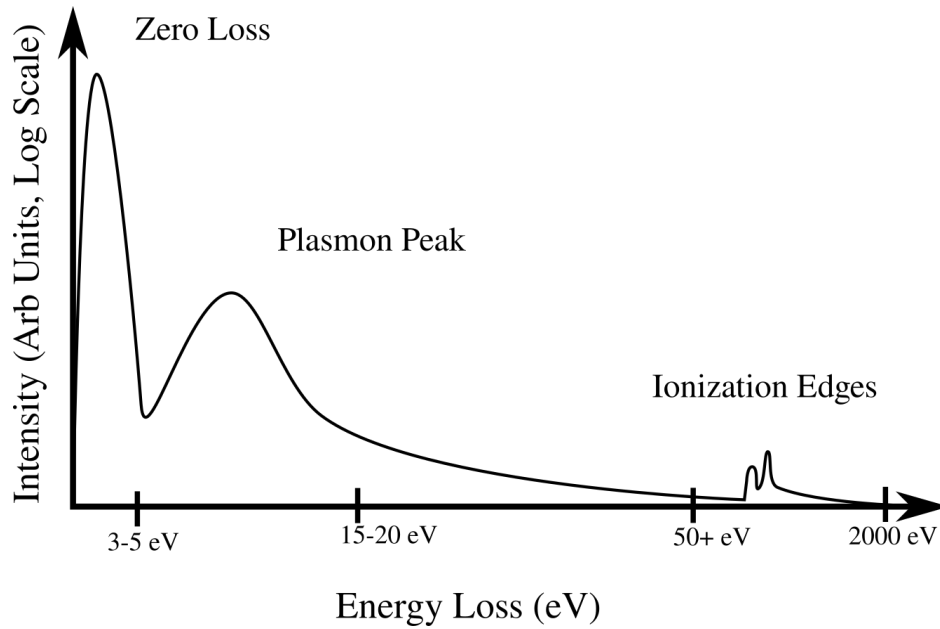


Figure 2.4: Sample EELS spectra identifying the main features, the zero loss peak, plasmon peak and ionization edges with fine structure. The intensities are on a log scale, and span approximately 6 orders of magnitude between the zero loss and the ionization edges.

- **Zero Loss Peak (ZLP):** The majority of the electrons in EELS pass through the specimen without experiencing an inelastic interaction, and retain their initial energy. The width of the ZLP defines the resolution of the spectrum and is due to energy spreading as the beam passes through the electron lenses [22]. For thin samples, the ZLP is also the most intense feature on a spectrum [11].
- **Background:** Beam electrons can excite loosely bound electrons close to the Fermi level into the unoccupied conduction band. Due to the large number of possible transitions and the fact that high energy events are less favourable, this results in a smoothly decaying background [11].
- **Plasmon Peak:** The electron beam can excite multiple atoms in a solid collectively, creating a wavelike oscillation in the electron cloud of the solid [11]. These are called plasmon excitations and result in a peak appearing between 5eV-30eV [11]. The shape and intensity of the plasmon peak is dependent on the bond strength of the material and can be used to probe properties such as thickness and surface topology [23; 24].
- **Ionization Edges:** Beam electrons can excite core electrons in a sample to the conduction band. As an atom's core states are in general, isolated from its surroundings, the "edges" for each element will occur at specific energy locations, independent of sample, analogous to characteristic x-rays [11]. These can be used to determine sample composition [11].

The array of independent interaction mechanisms occurring in EELS opens the possibility of beam electrons undergoing multiple inelastic events in the sample, referred to as plural scattering. In order for meaningful data to be extracted from a spectra, plural scattering must be minimized [11]. This is achieved by using samples thinner or at least comparable to the path length of the beam electrons [11]. If samples are too thick, duplicate plasmon peaks appear which drown out the relatively weaker ionization edges see Fig 2.5. Consequently, samples must be made thin enough to analyze the more sensitive parts of EELS spectra,

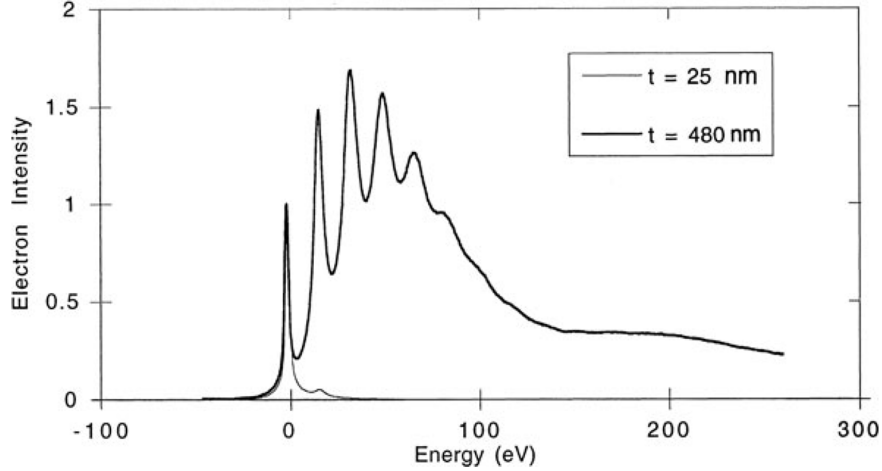


Figure 2.5: Two spectra demonstrating the importance of thin samples and single scattering events. In the thicker sample, plural scattering results in multiple evenly spaced plasmon peaks with intensities larger than the zero loss extending well past 100eV. The high background from the plasmon peaks and the thicker sample drown out any structure due to ionization edges [11]. Taken from Egerton, 2011 [11]

amongst others near edge structure.

Near Edge Structure

Ionization edges in EELS possess features extending up 50 eV beyond the onset of the edge, referred to as energy loss near edge structure (ELNES) [11]. These features are a reflection of the unoccupied states in the conduction band that represent the final states available to sample electrons. The band structure of the conduction band is largely dependent on the local bonds of the atom in question. Because of this, ELNES can be used to investigate properties dependent on the local environment of each element. Crystal structure is one such property, and ELNES can be used to distinguish different crystal structures of the same element such as carbon in graphite vs diamond, see Fig 2.6 [25]. ELNES is also sensitive to impurities or dopants that would effect the band structure [26]. The large decay in intensity with increasing energy seen in Figure 2.4, limits the useful range ionization edges to

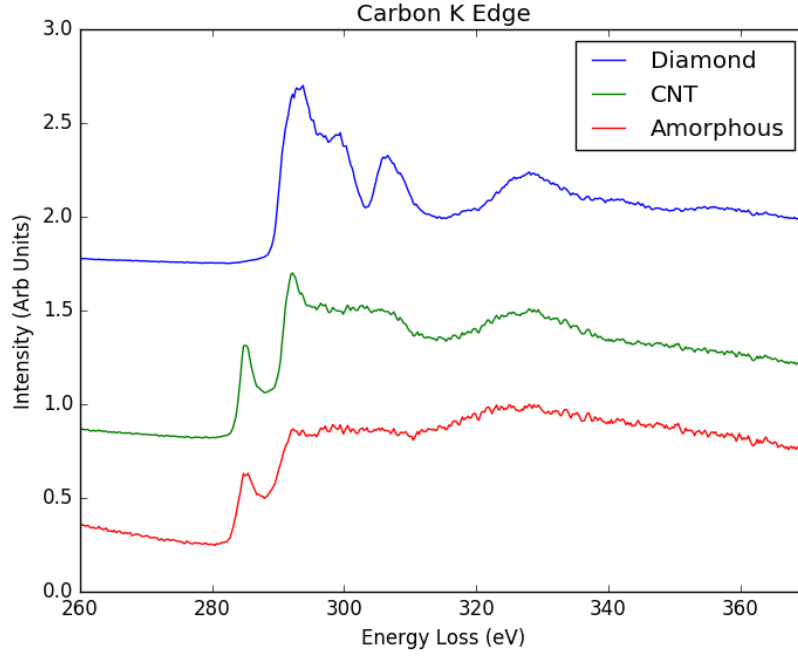


Figure 2.6: Carbon K edge taken at 30keV at McGill. The different crystal structures (amorphous, diamond and carbon nanotube) result in distinctly different ELNES which can be used for identification.

those less than $\sim 2\text{keV}$ which corresponds to approximately the K edge of silicon ($Z=14$) [27].

2.1.2 EELS in Experiment

In order to collect EELS spectra, electrons must pass entirely through the sample, making EELS a technique for transmission electron microscopes (TEM's)[11]. In order to collect these transmitted electrons and divide them according to energy, a magnetic prism is placed below the specimen to redirect the electrons into a detector, Fig 2.7. Inside the magnetic prism, there is a \mathbf{B} field perpendicular to the beam direction which exposes the transmitted electrons to a Lorentz force (bold text indicates vector quantities) [28]:

$$\mathbf{F}_B = q(\mathbf{v} \times \mathbf{B}) \quad (2.3)$$

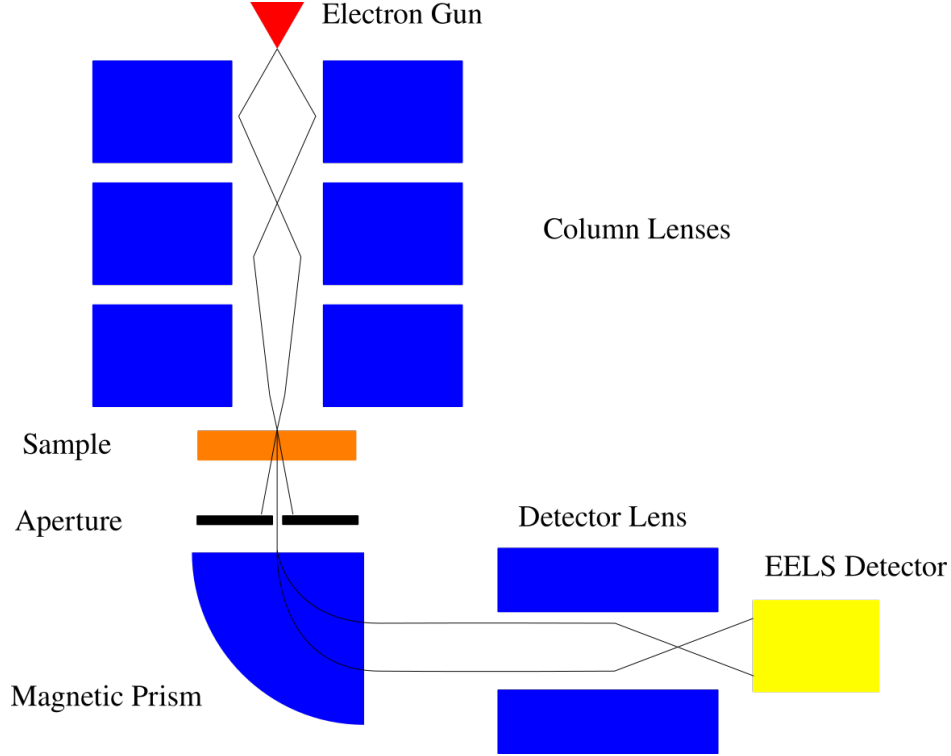


Figure 2.7: Experimental EELS setup, with the various magnetic lenses depicted in blue.

As the force varies according to the velocity of the electrons, the magnetic prism separates the electrons according to their energy:

$$\mathbf{F}_B = e(\mathbf{v} \times \mathbf{B}) = \frac{m\mathbf{v}^2}{\mathbf{r}} = \mathbf{F}_c \quad (2.4)$$

$$r = \frac{mv}{eB} = \frac{\sqrt{2mE}}{eB} \quad (2.5)$$

Where E is the energy of each electron after passing through the sample. Spectra are obtained by mapping each location on the detector to a corresponding energy loss value. Images are produced by rastering the beam over the sample and using the intensities of a specific energy loss value to create an image.

The quality of EELS results depends numerous factors in the microscope. Foremost among these is the quality of the electron beam. In order to obtain accurate results with regards to the finer features, the beam electrons must have very similar energies before

striking the sample, within a few eV. The larger this spread, the worse the energy resolution on the sample which obscures features in ELNES. The energy spread is largely dictated by the electron gun, with the choice for EELS being a field emission gun ($\delta E \sim 0.5 - 1\text{eV}$), as older style tungsten and LaB_6 guns are unsuitable for EELS with energy spreads greater than 2 eV [27]. The energy resolution can be further improved to the order of $\sim 10\text{meV}$ through the use of monochromators [29]. This improved energy resolution however comes at the cost of beam current which is another essential parameter for performing EELS. This is because sufficient signal needs to be collected to render the statistical \sqrt{N} errors small enough for features to become discernible. At higher energies, introducing a monochromator can result in a trade off between experimental error from the beam and statistical errors due to lack of counts. Lower current also translates into longer acquisition times, which expose the sample to more beam damage. In addition to the beam properties, EELS results also depend largely on the imaging mode being used in the electron microscope as is discussed below.

TEM vs SEM EELS

There are two main branches of electron microscopy: scanning electron microscopy (SEM) and transmission electron microscopy (TEM). TEM typically operates with beam energies between 100-300 keV designed to penetrate through thin samples, while SEM operates between 1-30 keV targeted towards analyzing bulk samples. Each method has its own advantages. The thin samples in TEM's result in a minimal interaction volume, far higher spatial resolution and have the ability to image individual atoms [9]. SEM's are optimized to scan the surfaces of samples and the large interaction volumes allow them to analyze bulk properties. SEM is also a more economical and flexible tool as it has far fewer sample requirements. EELS has been conventionally performed in TEM's as it requires the beam to pass through the sample and higher beam energies allow for thicker samples. Recent advances however have allowed EELS to be performed using an SEM with accelerating voltages of 30 keV [12]. As in a TEM, EELS in an SEM at 30keV requires thin samples, but offers the advantage of

reducing the beam damage which has been essential for investigating lithium materials.

2.1.3 Lithium in EELS

Lithium materials present a number of challenges to EELS analysis. Lithium ion battery materials are in general semiconductors with band gaps of varying sizes. Coupled with lithium's highly mobile nature, lithium materials are highly sensitive to electron beam damage. When performing analysis, damage results from the charge buildup when an electron beam passes through a sample. In electron conductive samples (eg. metals), this charge can be dissipated to some extent, however in materials with a band gap (eg. insulators, battery cathodes), the charge can displace lithium ions and break down the crystal structure. Lithium's high mobility also makes it vulnerable to knock on damage. This effect occurs when an electron interacts inelastically with an atom's nucleus and results in sufficient momentum transfer to displace it from its lattice site. Lithium is particularly vulnerable to this interaction because it requires only a small amount of energy ($\sim 0.2 - 3\text{eV}$) to displace it through a crystal [30]. Lithium's sensitivity to the beam make EELS's short acquisition times, on the order of seconds, well suited for its analysis. Recent developments enabling EELS at 30keV have made it applicable to a new range of lithium materials.

Beyond the experimental essentials, EELS analysis of lithium materials is complicated by lithium's only ionization edge being located at $\sim 55\text{eV}$. 55eV is at the boundary of what is considered reasonable for analysis as it lies close plasmon peak. The decay of the plasmon peak complicates background subtraction and makes it highly vulnerable to sample thickness and plural scattering. This energy range also often results in overlap between the lithium K-edge and the $M_{2/3}$ and M_4 edges of transition metals. In particular, the edges of Mn, Fe and Ni, all fall between 40-70eV. As these elements are key components to cathode materials, they can require further steps for analysis to be possible.

2.1.4 Preprocessing

There are two key steps to be performed upon acquiring an ELNES spectra before it can be used for meaningful conclusions, background subtraction and deconvolution.

Background Subtraction

The smooth decaying background in EELS spectra needs to be removed in order to isolate and analyze ELNES. However, the EELS background does not decay at a fixed rate and varies with energy and based on the presence of edges [31]. Consequently, it is not possible to fit a single function to an entire spectrum. Instead, the method of choice relies on fitting to a window directly before an ionization edge and refitting for each edge as needed. The most prevalent function used for this purpose is a power law decay [11]:

$$I_{bg} = AE^{-r} \quad (2.6)$$

Where E is the energy loss and A and r are fitting factors, typically determined through a least squares procedure [27]. This method has limitations due to different regions of the spectra decaying at different rates, with r ranging from 2-6.5 [27]. A fit must therefore be performed for every feature being analyzed in a spectrum [32; 33]. A downside of this method is the dependency on the size and location of the fitting window which results in unstable fits, as shown in Fig 2.8. Difficulty in removing the background is further complicated in situations when edges overlap or when attempting quantitative analysis. Coupled with the instability of power law fitting, this has resulted in a number of alternate models, such as polynomials, being proposed for specific cases. The power law method however, remains the most prevalent [32; 34].

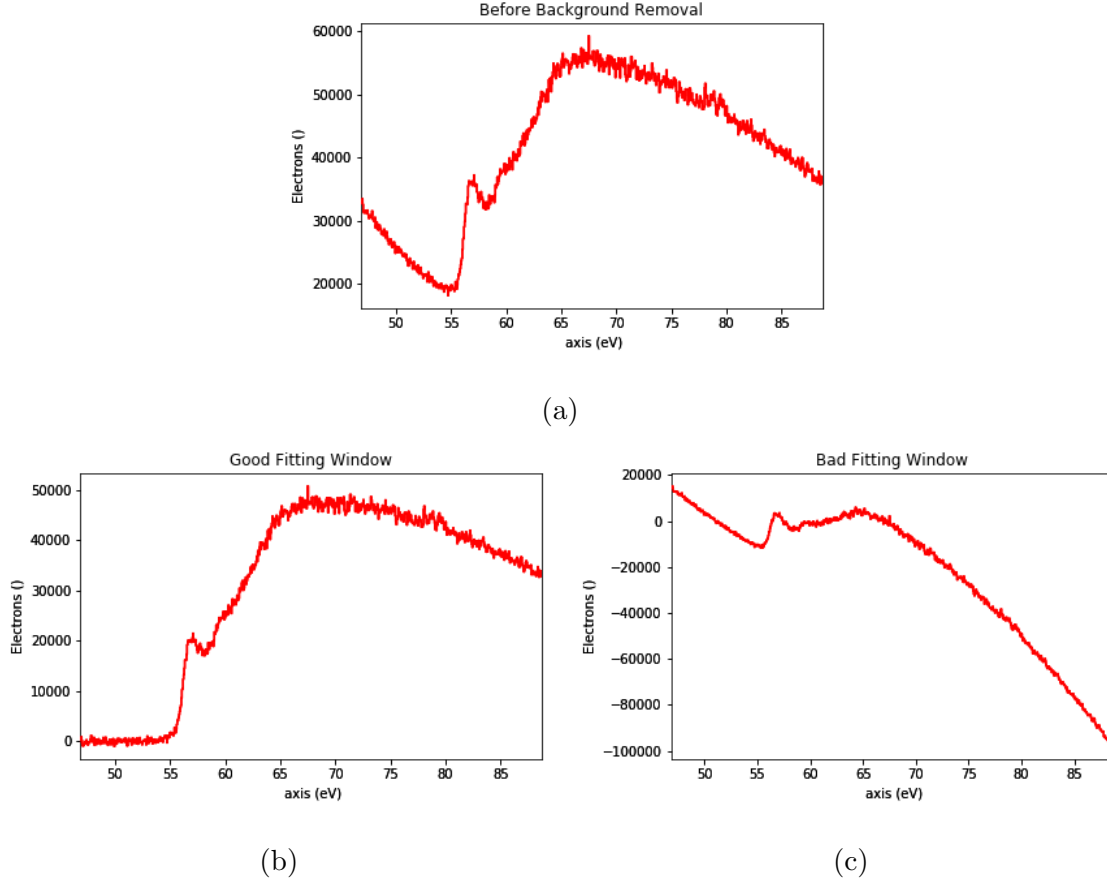


Figure 2.8: Results of power law background removal from raw spectrum (a) of metallic lithium K edge, using an appropriate (b) and inappropriate (c) window choices.

Deconvolution

Despite significant improvements in experimental equipment, there is still a degree of energy spread on beam electrons, typically in the range of $\sim 0.5\text{-}3\text{eV}$. This energy spread results in the observed ELNES on a spectra to be a convolution between the “actual” ELNES and the ZLP. Additionally, the probability plural scattering must also be addressed, as the low loss region of the spectrum is convoluted into the output spectra. In order to recover the single scattering spectrum, the output must undergo deconvolution. A number of techniques can be adopted for this purpose which can be split into either Fourier or Bayesian methods. Fourier techniques rely on describing the signal as a number of convolutions:

$$J(E) = Z(E) * [\delta(E) + \frac{S(E)}{I_0} + \frac{S(E) * S(E)}{2!I_0} + \dots] \quad (2.7)$$

Where $J(E)$ is the obtained spectra, $Z(E)$ is the zero loss peak, $S(E)$ is the single scattering spectra, and I_0 is the integrated intensity of the zero loss. The double scattering term is the convolution of the two single scattering terms, weighted by the decreased probability according to Poisson statistics. Taking a Fourier transform of this turns all of the convolutions into products:

$$j(\nu) = z(\nu) \left(1 + \frac{s(\nu)}{I_0} + \frac{s^2(\nu)}{2!I_0} + \frac{s^3(\nu)}{3!I_0} + \dots \right) \quad (2.8)$$

Which can in turn be collapsed into an exponential:

$$j(\nu) = z(\nu) \exp[s(\nu)/I_0] \quad (2.9)$$

This equation can then be solved for $s(\nu)$ and reverse Fourier transformed to obtain the single scattering spectra. In order to avoid amplifying the noise in the original spectra, represented by high frequency terms in Fourier space, the result must be broadened by a modifier. Thus, deconvolution can improve the energy resolution of the spectra only to a certain extent.

More recently, Bayesian methods have found success as well, in particular the Richardson-Lucy technique [35]. This technique is based on iterative methods initially developed in astronomy and used for the deconvolution of images, including those taken with the Hubble space telescope [36]. Similar to Fourier methods, the starting point is a convolution of the ideal spectra with the low loss, or point spread function ($R(E)$):

$$J(E) = R(E) * S(E) \quad (2.10)$$

As an EELS spectra is inherently pixilated by the CCD, the convolution can be transformed into a sum, defining the observed intensity at a pixel based on the intensity of the surrounding pixels:

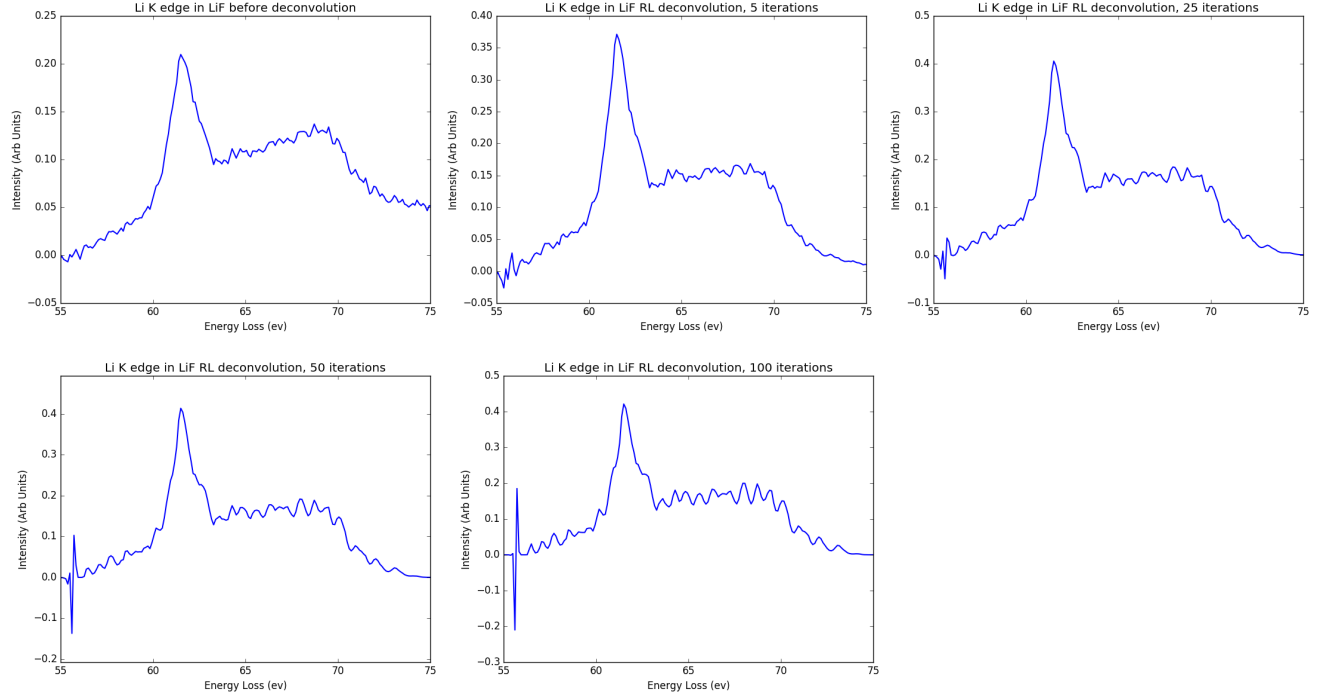


Figure 2.9: Effect of increasing iterations in Richardson-Lucy Algorithm. Iterations increase left to right, starting from the unprocessed background removed spectra on the top left, followed by 5, 25, 50, 100 iterations of deconvolution applied.

$$J(i) = \sum_j P(i, j) S(j) \quad (2.11)$$

Where $P(i, j)$ defines how much the intensity at pixel j affects pixel i . From here, the Richardson-Lucy algorithm applies Poisson statistics and iteratively calculates the single scattering spectra as [35]:

$$S^{k+1}(j) = S^k(j) \left(\frac{\sum_i \frac{P(i, j) J(i)}{\sum_l P(i, l) S^k(l)}}{\sum_i P(i, j)} \right) \quad (2.12)$$

Where k is the iteration number. As with Fourier methods, the final spectra cannot gain any more information, increasing iterations results in increased noise and artifacts as well, see Fig 2.9.

2.1.5 Other Experimental Techniques

EELS is not the only experimental technique available for the analysis of material microstructure, nor is it even the only electron microscopy technique available for the task. Other techniques capable of obtaining somewhat comparable results to EELS include x-ray based analysis such as x-ray absorption spectroscopy and energy dispersive spectroscopy. The following paragraphs briefly describe these methods and compare them to EELS.

X-ray Absorption Spectroscopy (XAS)

XAS operates on a similar principle to EELS. However, instead of probing the sample with an electron probe, a beam of x-rays is directed through the sample and like EELS the resulting energy losses in the output spectrum are binned [37]. This difference in probe type does not effect the measured quantity which is the same as in EELS: the unoccupied density of states of the material [37]. Because of their similarities, parallels have been drawn between EELS and XAS when developing theories. XAS however is typically used to measure far larger energy losses (> 5 keV) and consequently has limited applicability to lithium [38]. The most significant benefit of XAS is it's superior energy resolution (~ 0.1 eV) when compared to EELS (~ 1 eV) allowing for more features in near edge structures to be identified[11; 37]. This benefit comes at a cost however, XAS needs to be performed in a synchrotron, making it far more costly and less accessible to perform than EELS

Energy Dispersive Spectroscopy (EDS)

EDS is another form of analytic spectroscopy performed in electron microscopy. Unlike EELS and XAS which measure the unoccupied density of states, EDS measures the occupied DOS [15]. Like EELS, EDS probes the sample with an electron beam, but then collects the emitted x-rays produced when the sample electrons return to their relaxed states following excitation. These x-rays have the same characteristic energies as in EELS, but lack the resolution to distinguish fine structure. As such, it is limited to providing only composition information on samples. The benefit of EDS is less strict sample requirements as it does not

require the thin samples needed by EELS and can therefore be used to analyze both bulk and microscale features in samples [15].

2.2 Density Functional Theory (DFT)

Many of the results from EELS have non-intuitive interpretations, particularly in the case of ELNES which relies primarily on qualitative comparisons between measured and database spectra. Consequently, new materials require theoretical support to analyze results. This support often comes from ab initio calculations, such as density functional theory (DFT). This section describes the basis of DFT and its various implementations, as well as the peculiarities of simulating lithium materials.

2.2.1 DFT Background

DFT is an ab initio method that requires only atomic positions as input and is independent of experimental support. By solving a modified version of the Schrodinger equation, it is possible to obtain the ground state energy of the system, and from there determine a range of properties, including EELS spectra. This almost direct treatment of quantum mechanics makes DFT one of the most accurate techniques of first principle simulations. However, the quadratic to cubic scaling of the method limits its applicability to small scale systems, typical size limitations shown in Fig 2.10. DFT's accuracy and flexibility have resulted in the development of a large number (90+) of codes, both open source and commercial [39].

2.2.2 Formulation

DFT is centred on solving the many bodied Schrodinger equation [40]. The quantity in question is a solution for ψ_i , the electron wavefunctions from which observable properties can be calculated:

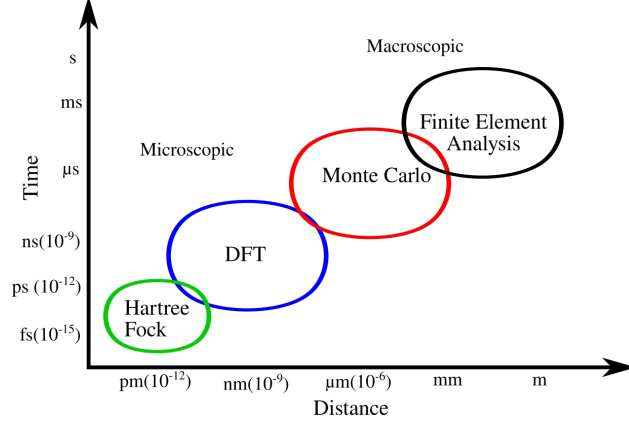


Figure 2.10: Various methods available to compute material properties and their corresponding regions of use.

$$-\frac{\hbar^2}{2} \sum_i^N \frac{\nabla^2 \psi_i}{m_i} + \sum_i^N V(\mathbf{r}_i) \psi_i = E \psi \quad (2.13)$$

In this case, the non-relativistic, spin independent, time independent case is considered, although more in-depth derivations can be found elsewhere [41]. The Born Oppenheimer approximation is now applied, which assumes that the nuclei can be separated from the electrons and will act classically. The validity of this assumption stems from the fact that nuclei are over 1000 times more massive than electrons [42]. Applying the Born Oppenheimer approximation results in only needing to solve for the ψ of electrons and allows the potential to be broken up:

$$\left[\frac{-\hbar^2}{2m_e} \sum_i^N \nabla^2 + \sum_i^N V(\mathbf{r}_i) + \sum_i^N \sum_{j<i}^N U(\mathbf{r}_i, \mathbf{r}_j) \right] \psi_i(\mathbf{r}_i) = E \psi_i \quad (2.14)$$

Where m_e is the mass of an electron, N is the number of electrons, and \mathbf{r}_i is a position vector. The terms inside the square brackets are collectively known as the Hamiltonian and are respectively: the kinetic energy of all the electrons, the Coulomb interaction between the electrons and the nuclei, and the electron-electron Coulomb interaction [40]. At this point, the equations are still too unwieldy to solve, depending on $3N$ variables (the position coordinates of each wavefunction), not to mention the many body problem lurking inside

the double sum. Facing this conundrum, the Hohenberg-Kohn Theorems are applied which postulate that [43]:

- The ground state *energy* of the system is a unique functional of the ground state *electron density*.
- The electron density which minimizes the overall energy corresponds to the real ground state electron density.

By changing the variables being solved for to the *density* and not wavefunctions, the problem is reduced down to only three variables: the three coordinates of the density field. The Hohenberg-Kohn theorems indicate that the observables can all be made into functionals of electron density and that any density other than the groundstate will result in a higher energy in the system [44]. The term functional is now defined as an object that acts like a function, except that it takes other functions as input instead of variables, eg:

$$F[f(x)] = f(x)^2 \quad (2.15)$$

In DFT, the relevant functional is the energy which is a functional of the density: $E[n(\mathbf{r})]$. Using the Hohenberg-Kohn theorems, it is possible to work towards a more manageable equation for energy as a functional of density by breaking down the potentials:

$$-\frac{\hbar}{2m_e} \sum_i \int \psi_i^* \nabla^2 \psi_i d^3r + \int V(\mathbf{r}) n(\mathbf{r}) d^3r + \frac{e^2}{2} \int \int \frac{n(\mathbf{r}) n(\mathbf{r}')}{|\mathbf{r} - \mathbf{r}'|} d^3r d^3r' + E_{\text{nuclei}} + E_{\text{XC}} = E[n(\mathbf{r})] \quad (2.16)$$

Where the second term is the energy from the electron density-nuclei interaction, the third term is the electron density-electron density Coulomb interaction and E_{nuclei} is the contribution from nucleus-nucleus interaction. The final term, E_{XC} is the exchange and correlation term, where all of the quantum features of the electrons are grouped the result of basing the analysis in terms of density. This equation cannot be directly solved from first principles by itself as a means is needed to obtain the electron density. On this front, the Kohn-Sham equations are introduced which assume that the electrons can be decoupled into single particle equations:

$$\left[T_i + V(\mathbf{r}) + V_H(\mathbf{r}) + V_{XC}(\mathbf{r}) \right] \phi_i(\mathbf{r}) = \epsilon_i \phi_i(\mathbf{r}) \quad (2.17)$$

Where ϕ_i and ϵ_i are the Kohn sham wavefunctions and eigenvalues respectively and V_H is the Hartree potential or:

$$V_H = e^2 \int \frac{n(\mathbf{r}')}{|\mathbf{r} - \mathbf{r}'|} d^3r' \quad (2.18)$$

The Hartree potential represents the interaction of the electron in question (the one at \mathbf{r} , not \mathbf{r}') and all the electrons in the sample. This results in some interaction between the electron and itself, a term that must be corrected for in the V_{XC} term. The Kohn-Sham equations can be readily solved, but require the density to calculate the Hartree potential. The density is in turn obtained from the wavefunctions:

$$n_{KS}(\mathbf{r}) = 2 \sum_i \phi_i^* \phi_i \quad (2.19)$$

Where the two is to account for electron spin. As the density is needed to calculate the wavefunctions and vice versa, a self consistent approach must be taken in order to obtain a valid result:

1. Assume a starting density
2. Use the initial density to calculate the Hartree potential and use it to solve the Kohn-Sham equations for the wavefunctions
3. Calculate a new density using Eq. 2.19.
4. Compare the new density to the initial, update the initial density.
5. Repeat steps 2-4 until the density converges and the energy is minimized. This density then represents the groundstate for the system.

This method is the starting point for DFT calculations, from which there are a number of variations with regarding how to proceed with these steps. Amongst these, the treatment of the exchange-correlation potential and choice of basis for the wavefunctions separate the various methods common in codes.

Exchange-Correlation Potential

The exchange-correlation potential was introduced above, but not defined. That is because there no easily solvable form for this term as it collects all of the unknown attributes not accounted for in the Kohn-Sham equations, including electron's being indistinguishable, the self interaction term, etc. There have been a number of proposed potentials, many designed for specific situations the most common of which will be discussed here. Like the potentials in the Kohn-Sham equations, the XC potential is defined as a functional of density. The various potentials vary according to accuracy and computational cost. The first attempt, originally proposed by Kohn and Sham in 1965 was the local density approximation (LDA) in which the XC potential depends only on the density [45; 46]:

$$E_{\text{XC}}[n(\mathbf{r})] = \int n(\mathbf{r})\epsilon_{\text{XC}}[n(\mathbf{r})]d^3r \quad (2.20)$$

LDA is exact in the case of a free electron gas and has obtained good success when applied to metallic solids. By also considering the gradient of the density, a more involved potential is obtained, called the generalized gradient approximation (GGA) [45; 47] :

$$E_{\text{XC}}[n(\mathbf{r})] = \int n(\mathbf{r})\epsilon_{\text{XC}}[n(\mathbf{r}), \nabla n[\mathbf{r}]]d^3r \quad (2.21)$$

Other parameters can also be taken into consideration, such as the potential energy (meta GGA) or empirical factors (hybrid functionals) [45; 48]. Depending on the desired property and available computing power, an appropriate functional should be chosen for each case.

Basis Sets

A second defining feature for various DFT methods is the choice of basis set for the wavefunctions, ϕ_i . A number of options have become prevalent in the available programs. These are divided into two distinct types, localized and periodic [40]. Localized basis sets rely on using orthogonal functions which decay rapidly away from the origin [40]. An example is Gaussian peaks, as is used in the Gaussian16 software package [49]. The very localized basis

set is useful for handling single, isolated molecules, which is ideally suited applications in quantum chemistry and biology. Poor scaling with electron number (typically N^3 or worse) limits the maximal size of system that can be studied [50]. In materials science, a typical system of interest is a bulk material and thus unsuitable for this approach. To handle these cases, periodic basis sets are used, by defining a unit cell and repeating it infinitely in all directions. The solution to the Schrödinger equation under these periodic boundary conditions is given by Bloch waves, defined as [51]:

$$\psi = u(\mathbf{r})e^{i\cdot\mathbf{k}} \tag{2.22}$$

Consequently, a natural basis choice for periodic boundary situations are plane waves, which are used in a number of DFT packages including VASP, Quantum Espresso, and Wien2k [52–54]. The periodic boundary method allows for accurate calculation of infinite samples representative of bulk materials. The computational limits then apply to the size of the unit cell, typically limited to at most a few hundred atoms [50]. These limits renders features such as defects and grain boundaries highly computationally expensive as they must be contained in a cell large enough to isolate them from their repeated images in adjacent cells. As large numbers of plane waves would be required to handle the fine features in the electron density close to nuclei, often an augmented plane wave (APW) technique is used. APW lowers the computational cost by dividing the unit cell into two regions: interstitial space and atomic basins (sometimes referred to as muffin tins), illustrated schematically in Fig 2.11 [54].

The ability to divide electrons into two groups is due to the fact that the core electrons surrounding each atom are largely unaffected by the local environment as they are screened by the outer shells [54]. The choice of which basis set is used inside the muffin tins provides additional options distinguishing DFT codes. One option is pseudopotentials, which are pre-generated densities for each element and can be varied to match the plane waves at the boundary [55]. The pseudopotential method is used in a number of codes, amongst others,

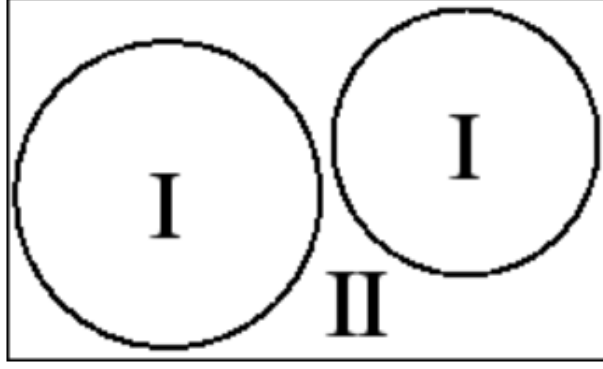


Figure 2.11: The two regions in an augmented plane wave approach. (I) Atomic Basins modelled with Pseudopotentials or atomic orbitals and (II) interstitial space modelled with a plane wave basis set. Taken from Schwarz *et al*, 2002 [54].

VASP and Quantum Espresso [52; 53]. Alternatively, spherical harmonics corresponding to the atomic orbitals can be used for increased accuracy [51]. This type of DFT is referred to as all-electron or full potential, as every electron is represented in the basis set, unlike the pseudopotential method where many are absorbed into the pre-calculated pseudopotential [54]. Fitting for all of the electrons in the sample comes at a computational cost, yet allows for more accurate analysis of the properties dependent on core states, such as ELNES spectra in EELS.

A flowchart demonstrating the various properties of some common DFT codes is illustrated in Fig 2.12. The DFT code used primarily in this work is Wien2k and is presented in the following section.

2.2.3 WIEN2k

WIEN2k is an all electron code that uses a linearized augmented plane wave (LAPW) formulation, combining plane waves with spherical harmonics illustrated in Fig 2.11 [54]. In WIEN2k's standard formalism, the basis sets for the Kohn-Sham wavefunctions can be represented as:

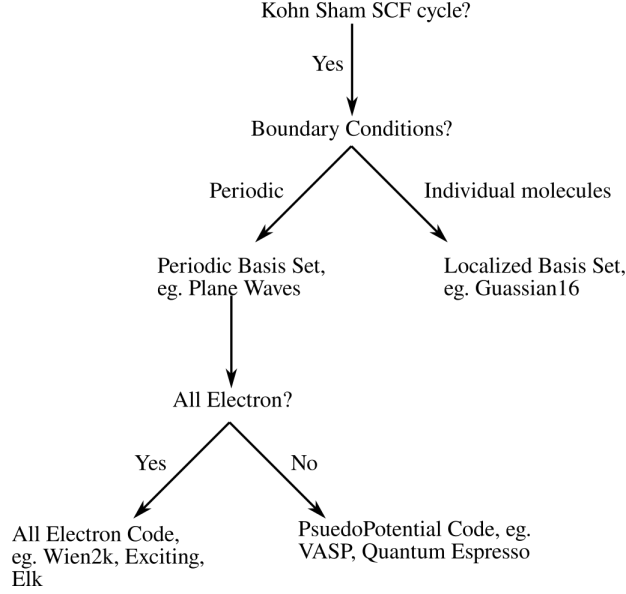


Figure 2.12: Flowchart depicting the various choices of basis set available to DFT codes.

$$\phi_{\mathbf{k}_n} = \begin{cases} \Sigma_{lm} [A_{lm,\mathbf{k}_n} u_l(r, E_l) + B_{lm,\mathbf{k}_n} \dot{u}_l(r, E_l)] Y_{lm}(\hat{\mathbf{r}}) & r \leq r_{\text{RMT}} \\ \frac{1}{\sqrt{\omega}} e^{i\mathbf{k}_n \cdot \mathbf{r}} & r > r_{\text{RMT}} \end{cases} \quad (2.23)$$

Where $Y_{lm}(\hat{\mathbf{r}})$ are the spherical harmonics and $u_l(r, E_l)$ are the solutions to the radial Schrödinger equation. The coefficients A_{lm,\mathbf{k}_n} and B_{lm,\mathbf{k}_n} are set to match the value and slope of the plane waves at the boundary [54]. The use of an all electron code is essential for computing EELS accurately as it allows for a more flexible treatment of the core electrons not granted in pseudopotential codes.

2.2.4 Quantum Theory of Atoms in Molecules

Before continuing to the application of DFT to EELS, a more direct application of DFT is briefly presented: defining atoms and bonds from the electron density. Initial work on this front was performed by Bader [56]. The electron density can be divided into regions, with each atomic basin delimited by surfaces satisfying [57]:

$$\nabla \rho(\mathbf{r}) \cdot \mathbf{n}(\mathbf{r}) = 0 \quad \forall \mathbf{r} \in S(\Omega, \mathbf{r}) \quad (2.24)$$

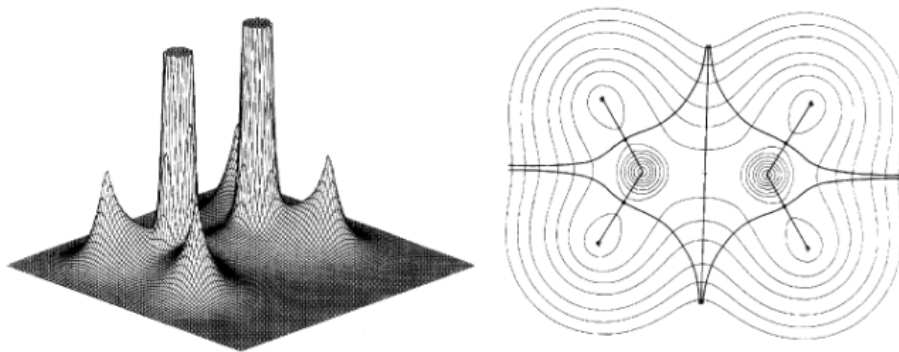


Figure 2.13: Density plot (left) and identification of atomic basin (right) in diborane atomic. From Bader, 1998 [56].

That is, surfaces with no flux of electron density through them which can be pictured as a “valleys” in the electron density “landscape,” see Fig 2.13. In order to rapidly calculate the location of these surfaces, critical points in the density field are located, satisfying $\nabla\rho(\mathbf{r}) = 0$. These critical points will always satisfy Eq. 2.24. With the exception of critical points at maximas in $\rho(\mathbf{r})$ which are located at nuclei, all of the critical points lie on interatomic surfaces [58]. The nature of the critical points can then be evaluated (minima, first or second order saddle point), and the location of bonds which are centred on first order saddle point critical points, can be determined [58]. The bonds can then be characterized to provide first principles chemical bonding analysis for quantum chemistry [59].

2.2.5 Lithium in DFT

Lithium’s low atomic number requires a number of special treatments in DFT. These are mainly due to its loosely bound electrons with large orbitals resulting from lithium’s small nuclear charge. Even the 1s level electrons in lithium can have orbitals extending well past 2.5 Bohr from the nuclei, far further than in heavier elements, see Fig 2.14 where a range of orbital sizes are compared [13]. This results in a number of issues. One of these is that it is difficult and sometimes impossible to set the atomic sphere radii large enough to contain all these 1s core electrons. As atomic spheres cannot overlap, they are typically limited to \sim

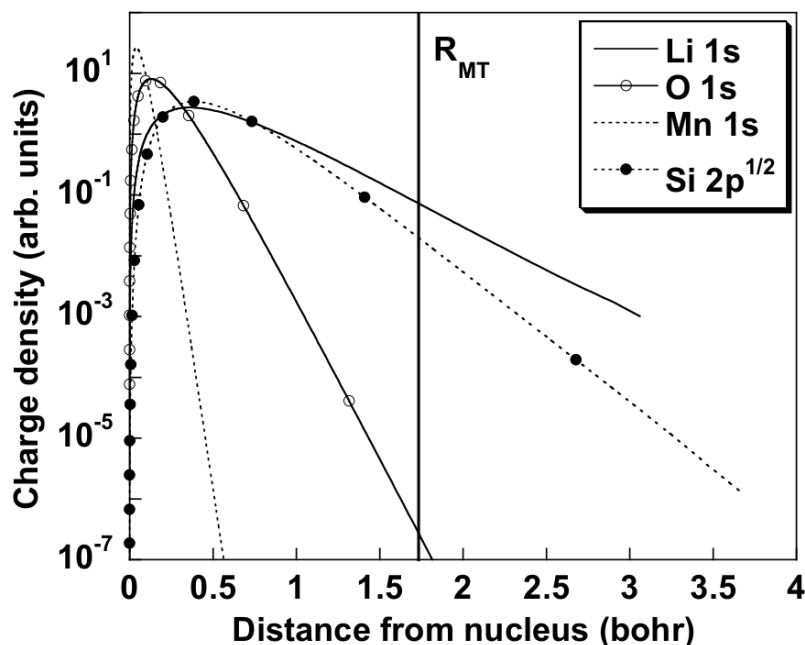


Figure 2.14: Orbital charge densities as a function of distance from nucleus, demonstrating the varying degrees of localization. From Mauchamp *et al*, 2006 [13]

2.0 Bohr. Depending on the compound, the sphere size can be further constrained as all the spheres must be roughly the same size (within 30%) [54]. If the sphere sizes are too varied, convergence time and accuracy can deteriorate dramatically. The alternative to large sphere size is to allow a degree ($\sim 0.5\%$) of core leakage into the calculation [54]. The downside to allowing leakage is that it may result in non physical effects at later stages in the calculation, or in the appearance of “ghostbands” in the calculation [54].

2.3 EELS Calculations

Having described the inner workings of EELS and DFT, the means to use the ground state density and the Kohn-sham wavefunctions and eigenvalues to calculate EELS spectra are discussed. Central to this challenge is the fact that DFT is a ground state theory; the Hohenberg Kohn theorems only guarantee that agreement between the calculation and reality

for the lowest energy state [43]. As EELS inherently involves exciting an atom above its ground state, assumptions must be made to address this issue. The various approaches to the issue of handling excitations are defining attributes of the various techniques used to calculate EELS. Additionally, the varying requirements of the wide array of EELS spectra features further diversify the techniques. Broadly, there are three methods for calculating EELS: multiple scattering, atomic multiplet and band structure methods. A number of the band structure methods as well as their advantages and applicability are described below.

2.3.1 Time Dependent Density Functional Theory -TDDFT

In TDDFT, the EELS spectrum is computed through the macroscopic dielectric function (ϵ_M). The method is centred on Fermi's Golden Rule, which is used to define matrix elements, which determine the probability of an electron being driven to a new state by a propagator:

$$M_{nm\mathbf{k}} = \langle n\mathbf{k} | e^{-i(\mathbf{q}+\mathbf{G})\mathbf{r}} | n'\mathbf{k}+\mathbf{q} \rangle \quad (2.25)$$

Where \mathbf{q} is the momentum transfer from the beam to the sample and \mathbf{G} is the Fourier coefficient of the probe. The initial and final states are the key parameters taken from DFT [60]. These matrix elements can be used to determine the independent particle polarizability χ^{KS} [60]:

$$\chi_{\mathbf{G},\mathbf{G}'}^{\text{KS}}(\mathbf{q}, \omega) = \frac{1}{V} \sum_{nm\mathbf{k}} \frac{f_{n\mathbf{k}} - f_{m\mathbf{k}+\mathbf{q}}}{\epsilon_{n\mathbf{k}} - \epsilon_{m\mathbf{k}+\mathbf{q}} + \omega + i\delta} M_{nm\mathbf{k}}(\mathbf{q}, \mathbf{G}) M_{nm\mathbf{k}}^*(\mathbf{q}, \mathbf{G}') \quad (2.26)$$

Where $f_{n\mathbf{k}}$ is the fermi distribution and V is the volume of the cell. χ^{KS} can be related to the reducible polarizability through the Dyson equation:

$$\chi = \chi_{\text{KS}} + \chi_{\text{KS}}(\nu + f_{\text{xc}})\chi \quad (2.27)$$

Where f_{xc} is the exchange and correlation potential. A common approximation is to set f_{xc} to zero, a method called the Random Phase Approximation (RPA) [61]. At this point two more approximations are introduced. \mathbf{q} is set to 0, referred to as the optical limit. This

assumes that the momentum transfer to the sample is minimal, an approach that is valid for low energy losses (< 50 eV). Secondly the probe wavelength is assumed to be much larger than the resulting perturbations, ($\mathbf{G} \rightarrow 0$). This is known as ignoring local field effects. Both approximations can be relaxed on a case by case basis, at increased computational expense [60]. With these approximations, first element of the dielectric tensor can be calculated as:

$$\epsilon_{00}^{-1}(\mathbf{q}, \omega) = 1 + v\chi \quad (2.28)$$

from which the macroscopic dielectric function can be obtained, which relates to the energy loss function ($L(\mathbf{q}, \omega)$):

$$[\epsilon_M(\mathbf{q}, \omega)]^{-1} = \epsilon_{00}^{-1}(\mathbf{q}, \omega) \quad (2.29)$$

$$L(\mathbf{q}, \omega) = -\text{Im}[\epsilon_M(\mathbf{q}, \omega)]^{-1} \quad (2.30)$$

The energy loss function is what is directly measured by EELS and is the standard of comparison for TDDFT. TDDFT is accurate for low losses, so ideal for calculations of plasmons, and in the limit of the optical approximation low energy M edges of transition metals and the lithium K edge [14]. Limitations of the approach are that it is based on the final state rule, and is consequently susceptible to excitonic effects in $\langle f |$. Additionally, local field effects can require subtle interpretations and may require additional computational cost [14]. TDDFT is also applicable to x-ray absorption spectroscopy where the optical limit is more valid. The only required modifications to the theory are a modification to the propagator in Eq. 2.25 [62]:

$$e^{i\mathbf{q}\cdot\mathbf{r}} \rightarrow e^{i\mathbf{k}\cdot\mathbf{r}} \epsilon \cdot \mathbf{r} \quad (2.31)$$

2.3.2 Cross Section Approach

TDDFT is a suitable choice for low loss EELS. For higher energy ionization edges with non-negligible momentum transfer, Fermi's Golden Rule can be used to compute a double differential cross section instead of the dielectric function. The differentials are with respect

to energy and scattering angle, the two relevant parameters in an EELS experiment. The relationship is given by [63]:

$$\frac{\partial^2 \sigma}{\partial \Omega \partial E} = \left[\frac{4\gamma^2}{a_0^2 q^4} \right] \frac{k_f}{k_i} \sum_{i,f} |\langle f | e^{i\mathbf{q}\cdot\mathbf{r}} | i \rangle|^2 \delta(E - E_f + E_i) \quad (2.32)$$

Where a_0 is the Bohr radius, E the energy loss and $\gamma = \sqrt{1 - \beta^2}$, the relativistic factor. As in TDDFT, the approach can be modified to solve for XAS, by replacing the Rutherford cross section with the Thompson cross section in the prefactor and changing the propagator according to Eq. 2.31.

The cross section formalism can be modified to account for anisotropic samples as well as some experimental parameters [63]. Similar to TDDFT, the essential parameters are the initial and final states, taken from DFT ($|f\rangle$ and $|i\rangle$). The simpler approach with fewer approximations can be attributed to the states being investigated: in low loss EELS, both the initial and final states depend heavily on the band structure, whereas for core losses the initial states are relatively constant and well defined [63]. Cross section methods however still suffer from the limitations of a one particle final state rule approach and their lack of ability to deal with excitonic effects.

2.3.3 Beth Salpeter Equations -BSE

The largest drawback of TDDFT and cross section calculations is the single particle formalism, which prevents proper treatment of excitonic effects. Solving the BSE is a two particle method that rigorously calculates the interaction between the excited electron and the resulting hole in the core state [64]. It is applicable to both low and core loss EELS calculations [60]. The core of the BSE is in solving the eigenvalue problem involving the effective two particle Hamiltonian [65]:

$$\hat{H}_{\text{eff}} |A_\lambda\rangle = E_\lambda |A_\lambda\rangle \quad (2.33)$$

The effective Hamiltonian can be broken into three parts, the diagonal, exchange, and correlation components[65]. The diagonal component accounts for single particle transitions:

$$H_{v\mathbf{c}\mathbf{k},v'\mathbf{c}'\mathbf{k}'}^{(\text{diag})} = (\epsilon_{c\mathbf{k}} - \epsilon_{v\mathbf{k}})\delta_{vv'}\delta_{cc'}\delta_{\mathbf{k}\mathbf{k}'} \quad (2.34)$$

The exchange component accounts for the repulsive interaction between the excited electron and its hole:

$$H_{v\mathbf{c}\mathbf{k},v'\mathbf{c}'\mathbf{k}'}^{(\text{x})} = \int d^3\mathbf{r} \int d^3\mathbf{r}' \varphi_{v\mathbf{k}}(\mathbf{r})\varphi_{c\mathbf{k}}^*(\mathbf{r})\bar{v}(\mathbf{r},\mathbf{r}')\varphi_{v'\mathbf{k}'}^*(\mathbf{r}')\varphi_{c'\mathbf{k}'}(\mathbf{r}') \quad (2.35)$$

Where φ are the single particle states of the hole and electron and \bar{v} is the unscreened Coulomb potential. Finally, the correlation component accounts for the attractive interaction between hole and electron:

$$H_{v\mathbf{c}\mathbf{k},v'\mathbf{c}'\mathbf{k}'}^{(\text{c})} = - \int d^3\mathbf{r} \int d^3\mathbf{r}' \varphi_{v\mathbf{k}}(\mathbf{r})\varphi_{c\mathbf{k}}^*(\mathbf{r})W(\mathbf{r},\mathbf{r}')\varphi_{v'\mathbf{k}'}^*(\mathbf{r}')\varphi_{c'\mathbf{k}'}(\mathbf{r}') \quad (2.36)$$

Where W is the screened Coulomb potential on the hole. By treating the hole created by the excited electron as a particle, solving the BSE produces superior results to single particle approaches, particularly in those with moderate screening [65]. However, this method is vastly more computationally demanding and can only be performed on the simplest of structures. This large computational trade off has led to the continued prevalence of single particle techniques.

2.3.4 Core Hole Approximation

The computational cost of the BSE method and the difficulties in handling excitonic effects in single particle approaches has resulted in additional approximations being made to improve single particle results. The most significant of these is the core hole approximation. This approximation is centred on artificially exciting the atom in question to an excited one in order to improve the final states in EELS, $\langle f|$. Early implementations involved replacing the excited atom with the next element on the periodic table, called the Z+1 approach [66]. This method was mildly successful, however it lacks the flexibility to handle excitations from

different shells, and has since been largely replaced with the core hole approximation [63]. The core hole approximation involves manually decreasing the occupancy of an excited state, and adding a charge to the background to conserve the electron number [54]. The effectiveness of the approximation has been mixed. In some cases, including a core hole results in excellent agreement with experiment, whilst in others, ignoring a core hole produces more accurate results. There have been a number of offered explanations based on the nature of the material: eg. insulators require a hole and metals do not. These general rules have not been successful in predicting all cases and more involved techniques based on density of states maps have also been proposed [67]. In general however, spectra tend to fall in between the two extremes, which has led to *ad hoc* approaches of including non integer core holes, so as to best fit experiment, see Fig 2.15 [63; 68–70]. This state of development has remained unchanged for the past 30 years and consistently led to unsatisfactory results [71–82].

The treatment of core holes is particularly problematic in lithium as its core states are very shallow, with only a single other core electron to shield it. The shallow shielded hole means that every lithium compound will exhibit some degree of core hole effects. Consequently, in order to calculate lithium ELNES, a more rigorous approach to core hole screening is required. Developing a deterministic method of introducing non-integer core holes for this end is the focus of this work

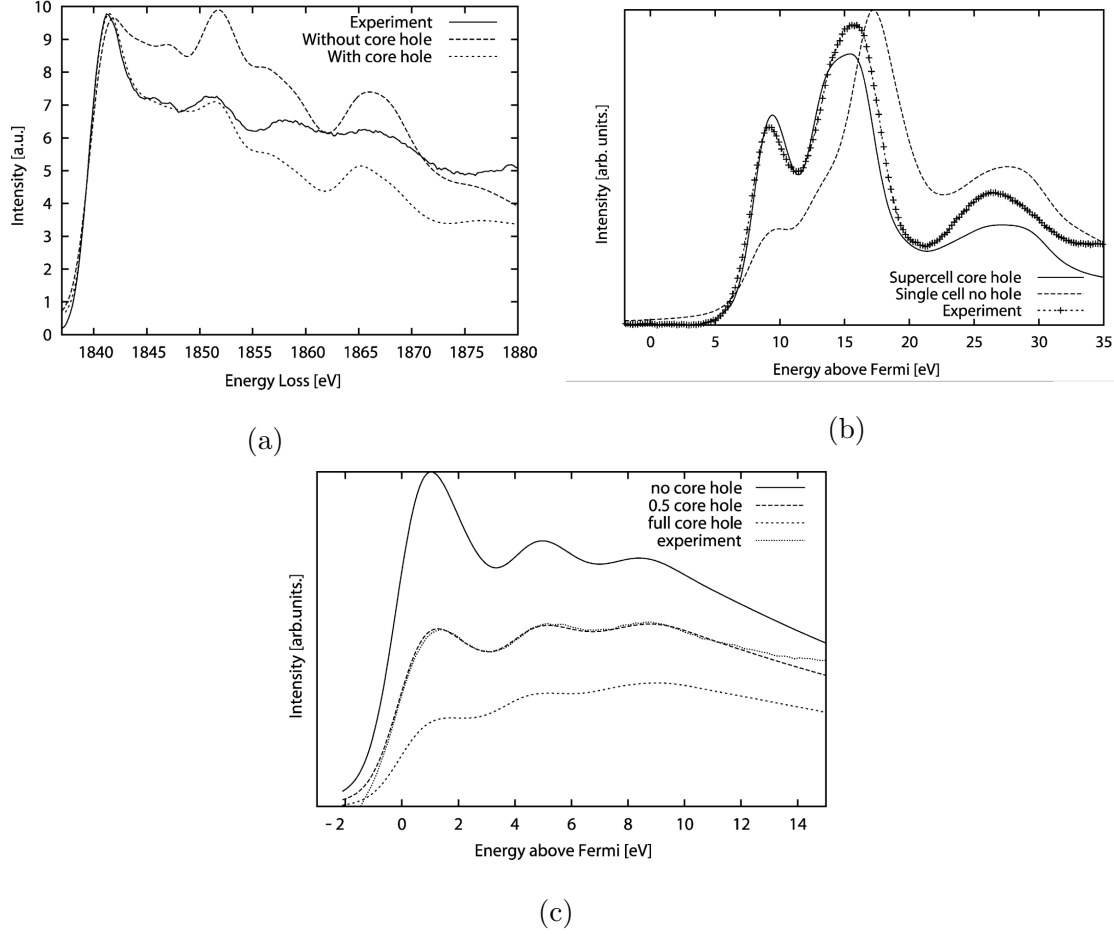


Figure 2.15: The three typical results of inserting a core hole. In (a) the core hole results in good agreement with experiment. In (b) and (c), the core hole overestimates the excitonic effects, resulting in errors in peak intensity. In (c), an *ad hoc* fractional core hole is inserted resulting in good agreement at the cost of physicality. Results from Herbert *et al*, 2003 (a,b) and Luitz *et al*, 2001 (c)[68; 69] .

Chapter 3

Methods

The lack of flexibility and accuracy of the core hole approximation combined with the computational deterrent of solving the BSE presents a barrier to expanding EELS calculations. Lithium in particular, being highly sensitive to these effects requires an improved method to continue EELS studies. To address this, a means of calculating the core hole shielding effect in lithium is developed. It is based in the single particle approach so as to reduce computational effort and does not require any empirical results. In this chapter the formulation and implementation of this method is discussed as well as the calculation and experimental parameters used in this work.

3.1 Improvement to Core Hole Shielding Calculations

To improve ELNES simulations, the core hole shielding contribution must be calculated. To maintain a low computational cost, the method developed here is based on a single particle approach. In particular, the relativistic cross section method using the final state rule (FSR, Eq. 2.32) [83]:

$$\frac{\partial^2 \sigma}{\partial \Omega \partial E} = \left[\frac{4\gamma^2}{a_0^2 q^4} \right] \frac{k_f}{k_i} \sum_{i,f} |\langle f | e^{i\mathbf{q}\cdot\mathbf{r}} | i \rangle|^2 \delta(E - E_f + E_i) \quad (3.1)$$

As mentioned in Section 2.3.4, shielding effects are contained in the $\langle f |$ term. These

effects originate from changes in the Hamiltonian arising from the introduction of a core hole and manifest themselves when solving for $\langle f |$ in the Kohn Sham equations (Eq. 2.17) [84]:

$$\left[T_i + V_{\text{ext}}(\mathbf{r}) + V_{\text{H}}(\mathbf{r}) + V_{\text{XC}}(\mathbf{r}) \right] \phi_i(\mathbf{r}) = \epsilon_i \phi_i(\mathbf{r}) \quad (3.2)$$

The core hole alters the Hartree and the exchange and correlation potentials, and this effect is reduced somewhat by shielding. The total change in the potential due to introduction of a core hole can be expressed as:

$$\Delta V_{\text{tot}}(\mathbf{r}) = \Delta V_{\text{H}}(\mathbf{r}) + \Delta V_{\text{XC}}(\mathbf{r}) = V_{\text{CH}}(\mathbf{r}) - V_{\text{S}}(\mathbf{r}) \quad (3.3)$$

where $V_{\text{CH}}(\mathbf{r})$ is the potential of a core hole and $V_{\text{S}}(\mathbf{r})$ represents the shielding potential. The current convention in literature when performing core hole calculations is to ignore this shielding term, despite the large effects it has been shown to have on ELNES. The shielding potential can be divided into two parts, core electron shielding $V_{\text{c}}(\mathbf{r})$ and valence electron shielding $V_{\text{v}}(\mathbf{r})$. Core shielding is due to electrons occupying core orbitals on the excited atom reducing how much the core hole can be “felt” outside of the atom. Valence screening is caused by valence and interstitial electrons being attracted to the positively charged hole. Neither of these terms are readily solvable for using current methods. When calculating ELNES for the lithium K edge, the core electron screening can be ignored. This assumption arises from lithium’s low electron count and simplifies the screening calculation considerably.

The valence electron screening can be calculated through linear response theory, as $\Delta V_{\text{H}}(\mathbf{r})$ and $\Delta V_{\text{XC}}(\mathbf{r})$ cannot be computed exactly [85]. Linear response theory relates changes in electron density to changes in potential, such as from the introduction of a core hole, as described by Shirley, Soininen and Rehr is [85]:

$$\Delta n(\mathbf{r}) = \int d^3\mathbf{r}' \chi^0(\mathbf{r}, \mathbf{r}'; \omega = 0) \Delta V_{\text{tot}}(\mathbf{r}') \quad (3.4)$$

Where χ^0 is the irreducible polarization function, given by $\chi^0(\mathbf{r}) = \delta n(\mathbf{r}) / \delta V(\mathbf{r})$. At this

point, the screening is set to zero ($V_S(\mathbf{r}) = 0$), to be reintroduced later as a perturbation. Restricting the region of interest to only the excited atom gives:

$$\Delta n_{\text{basin}} = \int_f d^3\mathbf{r} n_f(\mathbf{r}) - \int_i d^3\mathbf{r} n_i(\mathbf{r}) = -1 \quad (3.5)$$

Where the basin defining the integration limits is defined by Bader theory as described in Section 2.2.4. This equation indicates that, when there is no screening, the excited core electron has entirely left the basin, with no response from the material. Assuming that the polarization is constant inside this basin, lets the polarization to be calculated as:

$$\frac{\Delta n_{\text{basin}}}{V_{\text{CH}}} = \chi_{\text{basin}}^0 = \frac{\Delta n_{\text{basin}}}{\Delta V_{\text{tot}}} \quad (3.6)$$

Further assuming that the polarization is constant through changes in shielding potential, the shielding term can be reintroduced by perturbing the right hand side of Eq. 3.6 to obtain:

$$\frac{-1}{V_{\text{CH}}} = \frac{-1 + \delta n_{\text{basin}}}{V_{\text{CH}} - \delta V_v} \quad (3.7)$$

Which can be reduced to:

$$\frac{\delta V_v}{V_{\text{CH}}} = \delta n_{\text{basin}} \quad (3.8)$$

Equation 3.8 connects the screening due to valence electrons to a change in electron density, a rapidly calculable quantity. The screening potential is given in “units” of the core hole potential which allows the screening to be accounted for by modulating the occupancy of the core hole state. Additionally, while perturbed from the no screening case in Eq. 3.7, it should be noted that this argument holds when approached from the full screening case. This indicates that these approximations are valid over the entire range of screening cases ($\delta V_v = 0 \rightarrow V_{\text{CH}}$). The implementation of this theory in EELS calculations is discussed below.

3.2 Implementation

To calculate and implement the shielding term in Eq. 3.8, a series of calculations are performed. First, a standard DFT calculation is executed with no core hole, followed by one including a full core hole. Depending on cell size, the full core hole calculation is performed using a supercell so as to isolate individual core holes in the periodic boundaries. For both calculations, the electron occupancy inside the lithium atomic basin is calculated and used to calculate the screening potential according to Eq. 3.8. This returns a decimal value between 0 and 1 which is subtracted from the magnitude of the hole. A third calculation is then performed with using this non integer “shielded” hole, again using supercells as necessary.

3.3 Calculation and Experimental Details

Before discussing specific cases, it should be noted that all calculations were run in a manner to account for the peculiarities of lithium in DFT. In particular, atomic sphere radii on the lithium were maximized to minimize core leakage and monopole effects were verified to be negligible [13]. The standard DFT convergence tests (K points, RKmax) were also performed and all cells were relaxed according to volume. All supercells were performed in non conventional symmetries (eg. $P1$) so as to only produce a single core hole atom per cell and avoid any interaction between core holes. The final spectra are also converged based on supercell size. Density calculations are performed using Critic2 [58]. Detailed calculation and crystal parameters can be found in Appendix A.

All of the experimental results were obtained at McGill on a Hitachi SU900 FE-SEM. EELS spectra were acquired at 30 keV to minimize the beam damage to the lithium materials. All spectra had their backgrounds removed through a power law fit (see Section 2.1.4) and were deconvoluted using the Richardson-Lucy algorithm (also Section 2.1.4).

Chapter 4

Results and Discussion

Having developed a method and the means to implement screening calculations, ELNES are calculated for three common lithium compounds with a variety of properties; metallic lithium, LiF, and Li₂O. A mixed compound obtained after observing beam damage on LiF during a transformation into metallic lithium is also analyzed and discussed. Following results from the individual cases the overall effectiveness and applicability of the method is discussed.

4.1 Lithium Oxide

Li₂O is investigated first and screening calculations are performed as described in Section 3.2. After the initial two calculations, (with no hole then full hole), the density around the excited lithium atom is plotted before and after insertion of a core hole, see Fig 4.1.

The density plots clearly show valence electrons in the material being attracted to the excited atom. This response in the electron density indicates that core hole screening should have a noticeable effect on the final states. Additionally, the closest unexcited lithium atom in the density plot is largely unaffected by the core hole, in agreement with the supercell size being sufficient to isolate core holes. Calculating the difference in electron occupancy

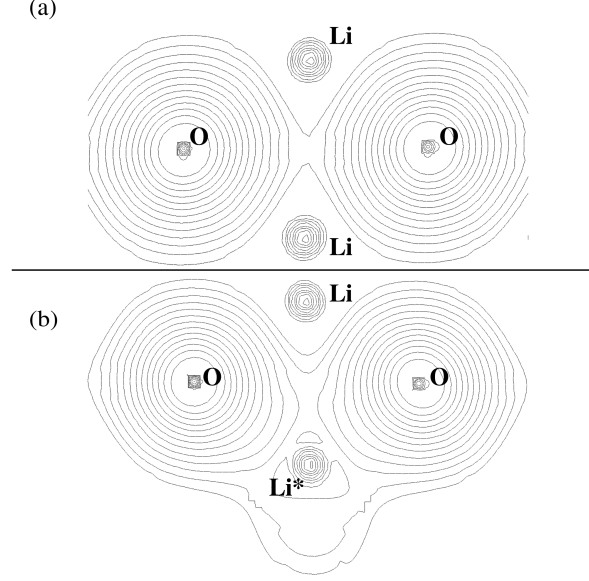


Figure 4.1: Effect of introducing a core hole in Li_2O . (a) no hole crystal. (b) Crystal with hole on starred lithium atom, inducing a response from the valence electrons. Contour lines on a logarithmic scale.

shows a decrease of 0.88 electron in the basin of the excited lithium atom. This decrease is smaller than would be expected in the no screening limit, and according to Eq. 3.8 indicates that the hole is 12% screened. A third calculation is performed using a correspondingly decreased hole size to obtain a final spectra. The K edge ELNES from all three simulations are compared to experiment in Fig 4.2.

In comparison to experiment, the full hole provides good agreement, as previously predicted in the literature [13]. However, the screened hole provides a superior result, which can be emphasized by measuring the ratio of the two peaks at $\sim 55\text{eV}$ and $\sim 58\text{ eV}$. A quantitative comparison of the values, presented in Table 4.1, reveals a dramatic improvement, decreasing the error from 20% to 6%.

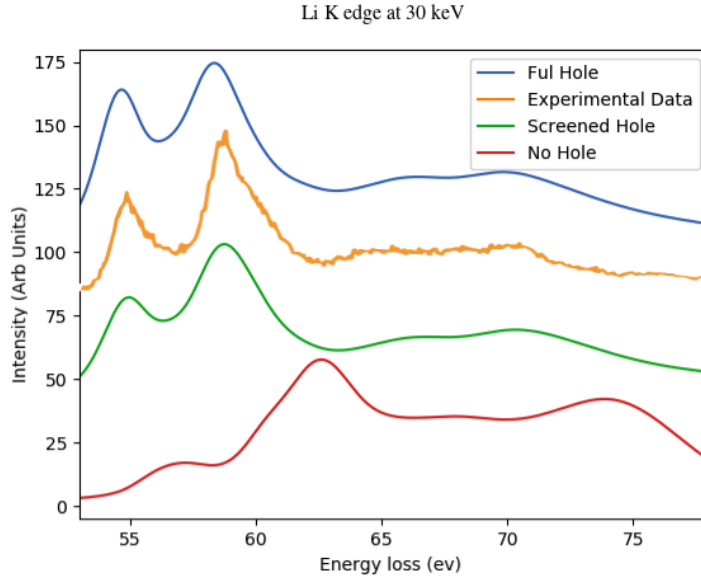


Figure 4.2: Lithium K edge of Li_2O from the three calculations taken with varying degrees of core hole.

Table 4.1: The ratio of intensities in the Li_2O spectra between the two peaks at 55 eV and 58 eV. Errors were calculated relative to experiment.

	Ratio	Error
Experiment	0.71	-
Full Hole	0.85	20%
Screened Hole	0.66	6%

4.2 Metallic Lithium

Metallic lithium has been predicted to exhibit no core hole effects due to a large degree of valence screening [86]. A density plot supports this notion, revealing that core holes attract a large number of neighbouring valence electrons, see density plot in Fig 4.3. The response to the excited atom is more aggressive than in Li_2O , implying a stronger screening impact. Calculating the screening factor reveals that the lithium core hole is $\sim 41\%$ screened, larger

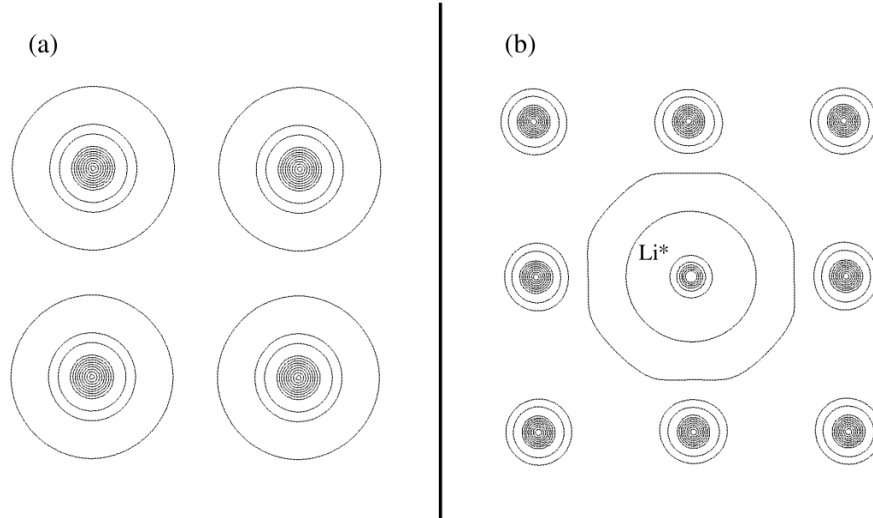


Figure 4.3: Electron density map of metallic lithium, before (a) and after (b) introduction of a core hole on the starred atom. The contours are on equal logarithmic scales.

than in Li_2O , but less than the full screening predicted in literature.

A comparison of the various core hole cases with experimental spectra is presented in Fig 4.4. The literature again predicts the superior agreement between full hole and no hole, but both are inferior to the screened hole result. Of particular note is the small peak located at ~ 58 eV, which is underestimated, in the no hole spectra, overestimated in the full hole, and correctly accounted for in the screened case. The only moderate (41%) screening goes against common convention in the literature that metals do not exhibit core hole effects. Other cases of metals requiring core holes have been previously highlighted such as the copper L_3 edge and the significant improvements observed with lithium suggest that screened core holes should be included or at least calculated in all cases [69]. It should be noted that lithium's lack of core electron screening may also contribute to the large core hole effects, which could be lessened for deep core states in heavier elements.

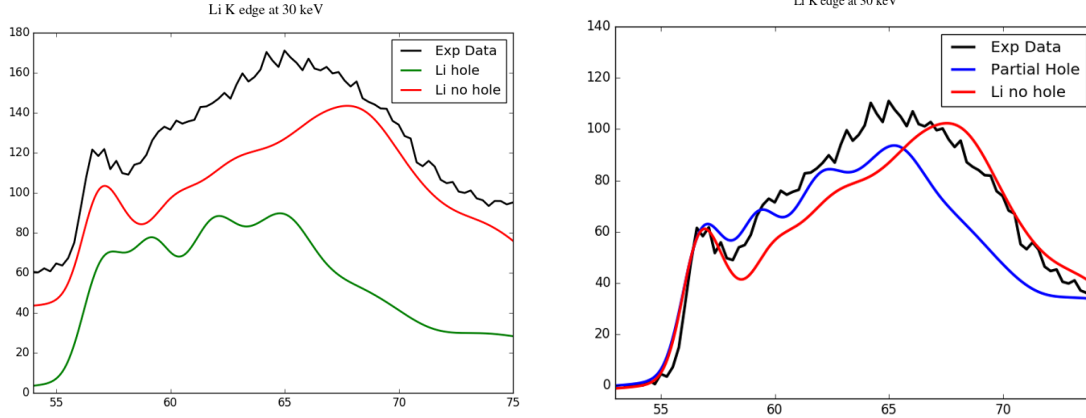


Figure 4.4: Lithium K edge of Li from the three calculations taken with varying degrees of core hole. On the left, the full and no hole results are presented, on the right the screened hole spectrum is compared to the no hole spectrum, both normalized to the experimental result at 56 eV. No vertical offset is applied on the right hand graph to better illustrate the differences between the spectra.

4.3 LiF

LiF has been one of the more published EELS results for lithium and simulations have obtained good agreement with a full core hole approximation [13; 87]. A qualitative probe of the electron density after introducing a core hole reveals lesser effects than observed in Li and Li_2O , see Fig 4.5. The introduction of a hole produces minor responses from the electron density, and these are largely limited to slight distortions in the fluorine electron clouds. Additionally, despite the loss of a core electron, the density around the excited lithium atom retains much of its initial form. The minimal effect of introducing a core hole is reflective of fluorine’s high electronegativity which “freezes” all of the electrons in place and minimizes valence electron screening. This effect is confirmed by calculating the screening coefficient which was determined to be zero in this case. Consequently, LiF represents the no screening case of Eq. 3.5 and the full hole spectra can be taken as the final spectrum. Plotting the spectra against experiment confirms that a full hole does indeed produce good agreement, Fig 4.6. The lack of screening in LiF also explains the good results obtained previously

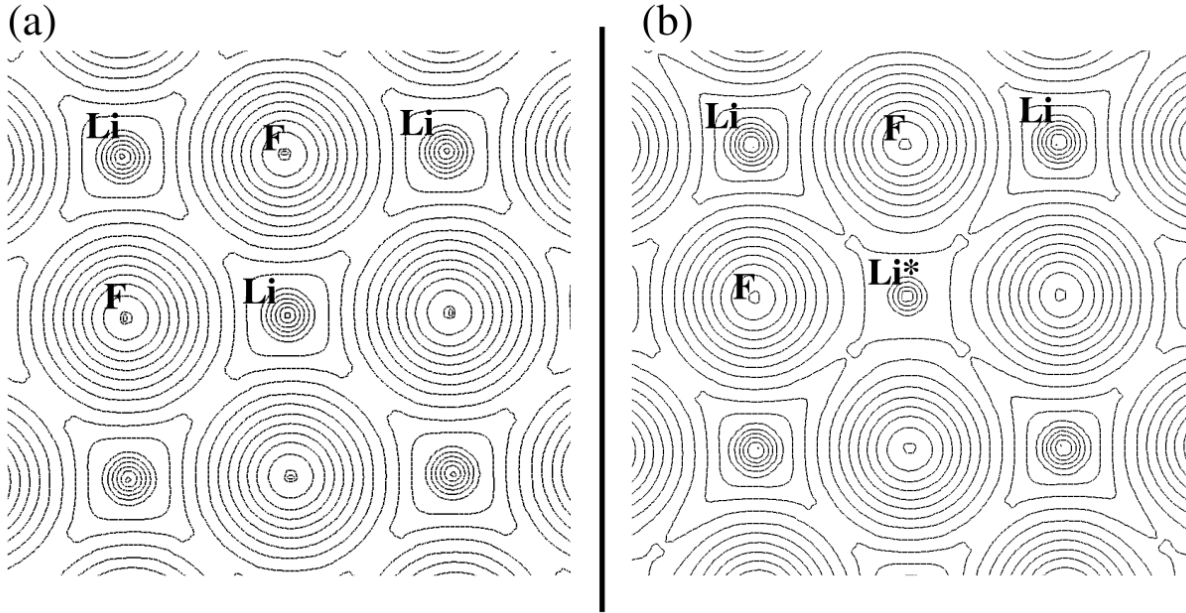


Figure 4.5: Electron density map of LiF, before (a) and after (b) introduction of a core hole on the starred atom. The contours are on equal logarithmic scales.

in literature when using only a full hole. It also supports the theory that inserting a full hole can be sufficient in the case of strong insulators, although again, lithium's lack of core electron screening may be contributing to this result.

4.4 Li-LiF Mixture

The full importance of including screening in core hole calculations is demonstrated when investigating a mixed phase crystal. When obtaining the spectra for LiF, a transformation to metallic lithium is observed, due to the beam damage. During this transformation, an acquired intermediate spectra displays both LiF and metallic lithium components. To investigate the transformation, a linear combination of the spectra from metallic lithium and LiF is compared to the experimental result, see Fig 4.7a. The good agreement obtained here supports both the inclusion of screening in metallic lithium and that the sample only contains only metallic lithium and LiF, with no intermediate phases or contamination. The

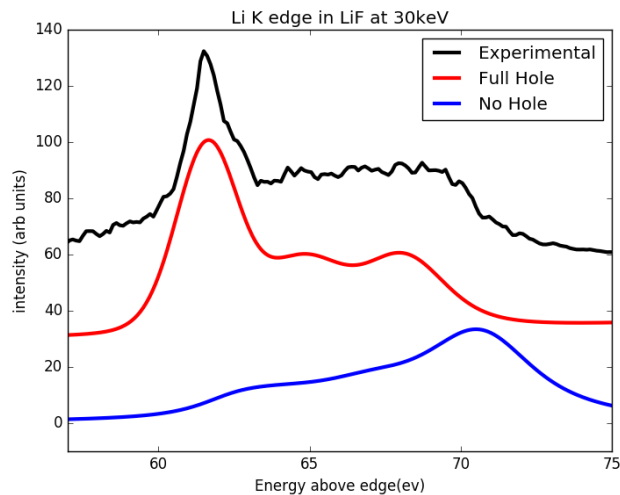


Figure 4.6: Lithium K edge of LiF from the two calculations taken with varying degrees of core hole.

importance of screening is highlighted in Fig 4.7b, where the no hole lithium spectra is used, resulting in a fit that fails to reproduce the peak at 59eV. This unaccounted for peak would prevent such an analysis from confirming the purity of the sample and of the mixture.

4.5 Discussion

The cases analyzed above highlight the importance of including a core hole and screening effects when calculating ELNES of the lithium K edge. In every case, a core hole was necessary, including metallic lithium which has been predicted to not exhibit core hole effects. Additionally, every case except LiF exhibited non negligible amounts of screening and applying the first order method developed in Chapter 3 results in dramatic improvements to experimental agreement. The impact of including screening in ELNES calculations is made more apparent when dealing with unknown cases such as the Li-LiF mixture where it is essential to fingerprinting the near edge structure. The improvement to the peak ratio in Li₂O is another key feature in terms of identifying oxidation on lithium edges, or taking the steps to quantitative analysis.

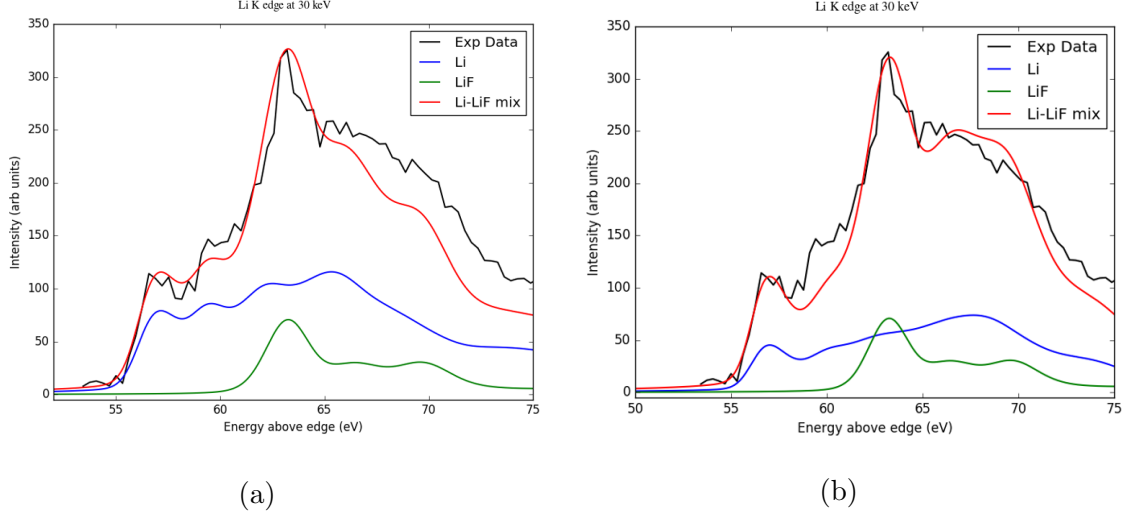


Figure 4.7: Lithium K edge of Li-LiF mix using full hole LiF spectrum and screened (a) and unscreened (b) Li spectrum.

Having improved upon the accuracy of the results, the effectiveness and applicability of the method is now discussed below. The screening calculations do not depend on any additional empirical data relative to standard DFT. Additionally, while three spectra are presented in each case for comparison (no hole, screened hole, and full hole), the technique predicts only a single correct result. The current method in literature of choosing between hole or no hole introduces a degree of uncertainty, as multiple correct spectra are predicted for each case. Any resulting disagreement can then be attributed to either screening effects or error and introduces a degree of uncertainty in the results. By only producing a single calculation which includes screening, this uncertainty is removed. Another major benefit to the method is that it scales at the same rate as conventional DFT. The largest computational cost occurs in the requirement to perform a third DFT calculations in order to obtain the screened result, an increase that scales at the same rate as the initial two calculations. Consequently, the method can be applied to any system that could be analyzed previously. It is also of note, that the shielding calculations presented in this work are implemented in the cross section band structure one of the more lightweight first principle methods of

calculating ELNES.

The success of the screening calculation when applied to lithium materials bring the generality of the approach into question. As mentioned in Section 3.3, core electron screening is ignored when calculating screening on the Li K edge. For the K edges of heavier elements this component will increase, altering the total screening potential and decreasing the valence electron screening. As is, the method is largely limited to the lithium K edge. The L/M edges of larger atoms may also see large improvements from this screening calculations, however, these cases become increasingly complex, as d-orbitals occupancy introduces a range of complications to the ELNES [88]. Consequently, in order to develop a approach to rapidly determine the screening coefficient in all cases, the core electron screening issue must be resolved.

On a final note, the reliable agreement between calculation and experiment helps solidify the validity of performing EELS at 30 keV to analyze beam sensitive materials. The obtained experimental results were successful in reproducing agreement with the literature predictions when ignoring screening effects. Finally, the ability to detect fine features such as the small second peak in metallic lithium and perform quantitative ratio analysis in Li_2O emphasize the benefits of this method in analyzing beam sensitive materials.

Chapter 5

Conclusion

The main objectives of this work have been to develop a better means to simulate EELS spectra in the context of lithium materials and further verify the reliability of EELS at 30 keV. The first order screening method presented in Chapter 3 is a step in the right direction. It represents a dramatic improvement to the current methods and results in superior agreement between simulation and experiment in every case treated in this work. Most importantly, the method achieves these improvements without requiring empirical data or *ad hoc* assumptions and maintains the computational scaling rate of previous methods. Ensuring that the method relies only on first principles enables it to reveal unintuitive results such as the unscreened hole in metallic lithium, and predict unknown systems such as the metallic lithium-lithium fluoride compound. The success of the method at matching the experimental 30 keV EELS is a strong argument for both the validity and potential of low energy EELS as a tool to analyze beam sensitive materials.

However, there is still considerable room for improvement in EELS calculations. Experimental equipment and techniques continue to advance to study more intricate materials. The screening calculations in this work were tailored to lithium's various peculiarities and restricted to crystalline materials. The improvements for lithium materials highlight the need for more general methods to support all elements, as well as amorphous and non infinite

samples. Additionally, the majority of theoretical EELS analysis remains qualitative and the realm of quantitative EELS presents an entirely new set of challenges. The ultimate goal of entirely predictive methods capable of performing quantitative analysis on any material remains out of reach and presents a target for future efforts.

Appendix A

Calculation Details

In this appendix detailed calculation parameters are presented for the lithium calculations performed in this work.

A.1 Crystal Structures

The unit cell crystal structures and atomic locations are presented below:

Table A.1: Cell parameters for Li_2O . Space group 225, $Fm\bar{3}m$, lattice parameter: 4.66Å

Atom	x	y	z
O	0.0	0.0	0.0
Li	0.25	0.25	0.25
Li	0.75	0.75	0.75

Table A.2: Cell parameters for metallic lithium. Space group Bcc, lattice parameter: 3.51Å

Atom	x	y	z
Li	0.0	0.0	0.0

Table A.3: Cell parameters for LiF. Space group 225, $Fm\bar{3}m$, lattice parameter: 4.057Å

Atom	x	y	z
Li	0.0	0.0	0.0
F	0.5	0.5	0.5

A.2 DFT Parameters

Table A.4: Calculation parameters used for ground and core hole state calculations of materials. Supercells were $2\times 2\times 2$ and used non-conventional symmetries to isolate core hole onto a single atom.

Case	K points	RKmax	RMT Li
Li	$17\times 17\times 17$	8.0	2.8
Li Supercell	$9\times 9\times 9$	8.0	2.8
Li ₂ O	$15\times 15\times 15$	8.0	2.0
Li ₂ O Supercell	$8\times 8\times 8$	8.0	2.0
LiF	$15\times 15\times 15$	8.0	2.0
LiF Supercell	$8\times 8\times 8$	8.0	2.0

Bibliography

- [1] Naoki Nitta, Feixiang Wu, Jung Tae Lee, and Gleb Yushin. Li-ion battery materials: present and future. *Materials Today*, 18(5):252–264, June 2015.
- [2] Vinodkumar Etacheri, Rotem Marom, Ran Elazari, Gregory Salitra, and Doron Aurbach. Challenges in the development of advanced Li-ion batteries: a review. *Energy & Environmental Science*, 4(9):3243–3262, 2011.
- [3] Xia Lu, Liang Zhao, Xiaoqing He, Ruijuan Xiao, Lin Gu, Yong-Sheng Hu, Hong Li, Zhaoxiang Wang, Xiaofeng Duan, Liquan Chen, Joachim Maier, and Yuichi Ikuhara. Lithium Storage in $\text{Li}_4\text{Ti}_5\text{O}_{12}$ Spinel: The Full Static Picture from Electron Microscopy. *Advanced Materials*, 24(24):3233–3238, 2012.
- [4] Zachary Arthur, Hsien-Chieh Chiu, Xia Lu, Ning Chen, Vincent Emond, Karim Zaghib, De-Tong Jiang, and George P. Demopoulos. Spontaneous reaction between an uncharged lithium iron silicate cathode and a LiPF_6 -based electrolyte. *Chemical Communications*, 52(1):190–193, 2016.
- [5] Simon Mller, Patrick Pietsch, Ben-Elias Brandt, Paul Baade, Vincent De Andrade, Francesco De Carlo, and Vanessa Wood. Quantification and modeling of mechanical degradation in lithium-ion batteries based on nanoscale imaging. *Nature Communications*, 9(1):2340, June 2018.
- [6] A. Van der Ven, G. Ceder, M. Asta, and P. D. Tepesch. First-principles theory of ionic diffusion with nondilute carriers. *Physical Review B*, 64(18):184307, October 2001.
- [7] Hsien-chieh Chiu, Nicolas Brodusch, Raynald Gauvin, Abdelbast Guerfi, Karim Zaghib, and George P. Demopoulos. Aqueous Synthesized Nanostructured $\text{Li}_4\text{Ti}_5\text{O}_{12}$ for High-Performance Lithium Ion Battery Anodes. *Journal of The Electrochemical Society*, 160(5):A3041–A3047, January 2013.

- [8] B. J. Inkson. Scanning electron microscopy (sem) and transmission electron microscopy (tem) for materials characterization. In Gerhard Hbschen, Iris Altpeter, Ralf Tschuncky, and Hans-Georg Herrmann, editors, *Materials Characterization Using Nondestructive Evaluation (NDE) Methods*, pages 17–43. Woodhead Publishing, 2016.
- [9] Thomas W. Hansen, Jakob B. Wagner, Poul L. Hansen, Sren Dahl, Haldor Topse, and Claus J. H. Jacobsen. Atomic-Resolution in Situ Transmission Electron Microscopy of a Promoter of a Heterogeneous Catalyst. *Science*, 294(5546):1508–1510, November 2001.
- [10] Shunsuke Kobayashi, Craig A. J. Fisher, Akihide Kuwabara, Yoshio Ukyo, and Yuichi Ikuhara. Quantitative analysis of Li distributions in battery material $\text{Li}_{1-x}\text{FePO}_4$ using Fe M2,3-edge and valence electron energy loss spectra. *Microscopy*, 66(4):254–260, August 2017.
- [11] RF Egerton. Eels in the electron microscope. *Springer, New York p*, 226, 1986.
- [12] Takeshi Sunaoshi, Yoshihisa Orai, Hiroyuki Ito, Takeshi Ogashiwa, Toshihide Agemura, and Mitsuru Konno. 30 kv stem imaging with lattice resolution using a high resolution cold fe-sem, 2012.
- [13] V. Mauchamp, F. Boucher, G. Ouvrard, and P. Moreau. Ab initio simulation of the electron energy-loss near-edge structures at the Li edge in Li , Li_2O , and LiMn_2O_4 . *Physical Review B*, 74(11):115106, 2006. WOS:000240872300038.
- [14] V. Mauchamp, P. Moreau, G. Ouvrard, and F. Boucher. Local field effects at Li K edges in electron energy-loss spectra of Li , Li_2O and LiF . *Physical Review B*, 77(4):045117, January 2008.
- [15] Joseph I. Goldstein, Dale E. Newbury, Patrick Echlin, David C. Joy, Charles E. Lyman, Eric Lifshin, Linda Sawyer, and Joseph R. Michael. *Scanning Electron Microscopy and X-ray Microanalysis*. Springer, Boston, MA, 2003.

- [16] Michael J. Rust, Mark Bates, and Xiaowei Zhuang. Sub-diffraction-limit imaging by stochastic optical reconstruction microscopy (storm). *Nature Methods*, 3(10):793–796, 2006.
- [17] Eugene Hecht. Optics. *Addison Wesley*, 997:213–214, 1998.
- [18] Alfredo M. Morales and Charles M. Lieber. A Laser Ablation Method for the Synthesis of Crystalline Semiconductor Nanowires. *Science*, 279(5348):208–211, 1998.
- [19] David B. Williams and C. Barry Carter. *Transmission electron microscopy: a textbook for materials science*. Springer, New York, 2nd ed edition, 2008.
- [20] Ludwig Reimer. Electron optics of a scanning electron microscope. In *Scanning Electron Microscopy*, Springer Series in Optical Sciences, pages 13–56. Springer, Berlin, Heidelberg, 1998.
- [21] Maria Varela, Jaume Gazquez, and Stephen J. Pennycook. Stem-eels imaging of complex oxides and interfaces. *MRS Bulletin*, 37(1):29–35, 2012.
- [22] Christian Colliex. An illustrated review of various factors governing the high spatial resolution capabilities in eels microanalysis. *Ultramicroscopy*, 18(1):131–150, 1985.
- [23] T. Malis, S. C. Cheng, and R. F. Egerton. Eels log-ratio technique for specimen-thickness measurement in the tem. *Journal of Electron Microscopy Technique*, 8(2):193–200, 1988.
- [24] Jaysen Nelayah, Mathieu Kociak, Odile Stphan, F. Javier Garca de Abajo, Marcel Tenc, Luc Henrard, Dario Taverna, Isabel Pastoriza-Santos, Luis M. Liz-Marzn, and Christian Colliex. Mapping surface plasmons on a single metallic nanoparticle. *Nature Physics*, 3(5):348–353, 2007.
- [25] Ann-Lenaig Hamon, Jo Verbeeck, Dominique Schryvers, Jan Benedikt, and Richard M. C. M. v d Sanden. Elmes study of carbon k-edge spectra of plasma deposited carbon films. *Journal of Materials Chemistry*, 14(13):2030–2035, 2004.

- [26] G. Torrisi, A. Di Mauro, M. Scuderi, G. Nicotra, and G. Impellizzeri. Atomic layer deposition of ZnO/TiO₂ multilayers: towards the understanding of Ti-doping in ZnO thin films. *RSC Advances*, 6(91):88886–88895, 2016.
- [27] Helmut Kohl and Ludwig Reimer. *Transmission Electron Microscopy: Physics of Image Formation*. Number 36 in Springer Series in Optical Sciences. Springer, New York, NY, 2008.
- [28] David J Griffiths. *Introduction to electrodynamics*. Pearson, 2013. OCLC: 794711764.
- [29] Jordan A. Hachtel, Andrew R. Lupini, and Juan Carlos Idrobo. Exploring the capabilities of monochromated electron energy loss spectroscopy in the infrared regime. *Scientific Reports*, 8(1):5637, April 2018.
- [30] Kisuk Kang and Gerbrand Ceder. Factors that affect Li mobility in layered lithium transition metal oxides. *Physical Review B*, 74(9):094105, September 2006.
- [31] H. Tenailleau and J. M. Martin. A new background subtraction for low-energy eels core edges. *Journal of Microscopy*, 166(3):297–306, 1992.
- [32] J. Verbeeck and S. Van Aert. Model based quantification of EELS spectra. *Ultramicroscopy*, 101(2):207–224, 2004.
- [33] R. F. Egerton. Inelastic scattering of 80 keV electrons in amorphous carbon. *The Philosophical Magazine: A Journal of Theoretical Experimental and Applied Physics*, 31(1):199–215, 1975.
- [34] T. Riedl, T. Gemming, and K. Wetzig. Extraction of EELS white-line intensities of manganese compounds: Methods, accuracy, and valence sensitivity. *Ultramicroscopy*, 106(4):284–291, March 2006.
- [35] A. Gloter, A. Douiri, M. Tenc, and C. Colliex. Improving energy resolution of eels spectra: an alternative to the monochromator solution. *Ultramicroscopy*, 96(3):385–400, 2003.

- [36] J. E. Krist. Deconvolution of hubble space telescope images using simulated point spread functions. *Astronomical Data Analysis Software and Systems I, A.S.P. Conference Series*, 25:226–227, 1992.
- [37] Frank de Groot. High-resolution x-ray emission and x-ray absorption spectroscopy, 2001.
- [38] Ian MacLaren, Kirsty J. Annand, Colin Black, and Alan J. Craven. EELS at very high energy losses. *Microscopy*, 67(suppl_1):i78–i85, 2018.
- [39] Codes - NOMAD, <https://www.nomad-coe.eu/externals/codes>, 2018.
- [40] David S Sholl and Janice A Steckel. *Density functional theory: a practical introduction*. Wiley, Hoboken, N.J., 2009. OCLC: 441874984.
- [41] E. K. U. Gross and K. Burke. *Time-Dependent Density Functional Theory*. Lecture Notes in Physics. Springer, Berlin, Heidelberg, 2006.
- [42] G. Grff, H. Kalinowsky, and J. Traut. A direct determination of the proton electron mass ratio. *Zeitschrift fr Physik A Atoms and Nuclei*, 297(1):35–39, 1980.
- [43] P. Hohenberg and W. Kohn. Inhomogeneous electron gas. *Physical Review*, 136(3B):B864–B871, 1964.
- [44] R G Parr. Density Functional Theory. *Annual Review of Physical Chemistry*, 34(1):631–656, 1983.
- [45] Jianmin Tao, John P. Perdew, Viktor N. Staroverov, and Gustavo E. Scuseria. Climbing the Density Functional Ladder: Nonempirical Meta–Generalized Gradient Approximation Designed for Molecules and Solids. *Physical Review Letters*, 91(14):146401, 2003.
- [46] W. Kohn and L. J. Sham. Self-Consistent Equations Including Exchange and Correlation Effects. *Physical Review*, 140(4A):A1133–A1138, 1965.

- [47] John P. Perdew, Kieron Burke, and Yue Wang. Generalized gradient approximation for the exchange-correlation hole of a many-electron system. *Physical Review B*, 54(23):16533–16539, 1996.
- [48] Axel D. Becke and Erin R. Johnson. A simple effective potential for exchange. *The Journal of Chemical Physics*, 124(22):221101, 2006.
- [49] M. J. Frisch et al. Gaussian16 Revision B.01, 2016. Gaussian Inc. Wallingford CT.
- [50] Stephan Mohr, Marc Eixarch, Maximilian Amsler, Mervi J. Mantsinen, and Luigi Genovese. Linear scaling DFT calculations for large tungsten systems using an optimized local basis. *Nuclear Materials and Energy*, 15:64–70, May 2018.
- [51] David J. Griffiths. *Introduction to quantum mechanics*. Pearson Prentice Hall, Upper Saddle River, NJ, 2005.
- [52] Paolo Giannozzi and Baroni. QUANTUM ESPRESSO: a modular and open-source software project for quantum simulations of materials. *Journal of Physics: Condensed Matter*, 21(39):395502, 2009.
- [53] Jrgen Hafner. Ab-initio simulations of materials using VASP: Density-functional theory and beyond. *Journal of Computational Chemistry*, 29(13):2044–2078, 2009.
- [54] K. Schwarz, P. Blaha, and G. K. H. Madsen. Electronic structure calculations of solids using the WIEN2k package for material sciences. *Computer Physics Communications*, 147(1):71–76, 2002.
- [55] David J. Singh and Lars Nordstrm. *Planewaves, Pseudopotentials, and the LAPW Method*. Springer, New York, NY, UNITED STATES, 2006.
- [56] Richard F. W. Bader. Atoms in Molecules. In *Encyclopedia of Computational Chemistry*. American Cancer Society, 2002.

- [57] Richard F. W. Bader. A quantum theory of molecular structure and its applications. *Chemical Reviews*, 91(5):893–928, 1991.
- [58] A. Otero-de-la Roza, Erin R. Johnson, and Vctor Luaa. Critic2: A program for real-space analysis of quantum chemical interactions in solids. *Computer Physics Communications*, 185(3):1007–1018, 2014.
- [59] Malte Fugel, Jens Beckmann, Dylan Jayatilaka, Gerald V. Gibbs, and Simon Grabowsky. A Variety of Bond Analysis Methods, One Answer? An Investigation of the ElementOxygen Bond of Hydroxides HnXOH. *Chemistry A European Journal*, 24(23):6248–6261, 2018.
- [60] Andris Gulans, Stefan Kontur, Christian Meisenbichler, Dmitrii Nabok, Pasquale Pavone, Santiago Rigamonti, Stephan Sagmeister, Ute Werner, and Claudia Draxl. exciting: a full-potential all-electron package implementing density-functional theory and many-body perturbation theory. *Journal of Physics: Condensed Matter*, 26(36):363202, 2014.
- [61] Claudia Ambrosch-Draxl and Jorge O. Sofo. Linear optical properties of solids within the full-potential linearized augmented planewave method. *Computer Physics Communications*, 175(1):1–14, 2006.
- [62] A. L. Ankudinov, B. Ravel, J. J. Rehr, and S. D. Conradson. Real-space multiple-scattering calculation and interpretation of x-ray-absorption near-edge structure. *Physical Review B*, 58(12):7565–7576, 1998.
- [63] C. Hebert. Practical aspects of running the WIEN2k code for electron spectroscopy. *Micron*, 38(1):12–28, 2007. WOS:000241994700002.
- [64] E. E. Salpeter and H. A. Bethe. A Relativistic Equation for Bound-State Problems. *Physical Review*, 84(6):1232–1242, 1951.

- [65] Stephan Sagmeister and Claudia Ambrosch-Draxl. Time-dependent density functional theory versus BetheSalpeter equation: an all-electron study. *Physical Chemistry Chemical Physics*, 11(22):4451–4457, 2009.
- [66] P. A. Lee and G. Beni. New method for the calculation of atomic phase shifts: Application to extended x-ray absorption fine structure (EXAFS) in molecules and crystals. *Physical Review B*, 15(6):2862–2883, 1977.
- [67] Vincent Mauchamp, Michel Jaouen, and Peter Schattschneider. Core-hole effect in the one-particle approximation revisited from density functional theory. *Physical Review B*, 79(23):235106, 2009.
- [68] J. Luitz, M. Maier, C. Hbert, P. Schattschneider, P. Blaha, K. Schwarz, and B. Jouffrey. Partial core hole screening in the Cu L3 edge. *The European Physical Journal B*, 21(3):363–367, 2001.
- [69] C. Hebert, J. Luitz, and P. Schattschneider. Improvement of energy loss near edge structure calculation using Wien2k. *Micron*, 34(3-5):219–225, 2003. WOS:000184846600012.
- [70] J. C. Slater. Energy Band Calculations by the Augmented Plane Wave Method**The research reported in this paper has been assisted by the National Science Foundation and the Office of Naval Research, as well as by the Army, Navy, and Air Force. *Advances in Quantum Chemistry*, 1:35–58, January 1964.
- [71] R. Brydson, J. Bruley, and J. M. Thomas. Further evidence for core-hole effects in the near-edge structures of light-element K-edges. *Chemical Physics Letters*, 149(4):343–347, 1988.
- [72] T. P. Hardcastle, C. R. Seabourne, D. M. Kepaptsoglou, T. Susi, R. J. Nicholls, R. M. D. Brydson, A. J. Scott, and Q. M. Ramasse. Robust theoretical modelling of core ionisation edges for quantitative electron energy loss spectroscopy of B- and N-doped graphene. *Journal of Physics: Condensed Matter*, 29(22):225303, 2017.

- [73] E. W. Tait, L. E. Ratcliff, M. C. Payne, P. D. Haynes, and N. D. M. Hine. Simulation of electron energy loss spectra of nanomaterials with linear-scaling density functional theory. *Journal of Physics: Condensed Matter*, 28(19):195202, 2016.
- [74] P. Jegadeesan, S. Amirthapandian, Gurpreet Kaur, Sharat Chandra, and B. K. Panigrahi. Characterization of MO bonds in Y₂Ti₂O₇ and Y₂TiO₅ with EELS. *physica status solidi (b)*, 252(1):206–211, 2015.
- [75] Damien Magne, Vincent Mauchamp, Stphane Clrier, Patrick Chartier, and Thierry Cabioch. Site-projected electronic structure of two-dimensional Ti₃C₂MXene: the role of the surface functionalization groups. *Physical Chemistry Chemical Physics*, 18(45):30946–30953, 2016.
- [76] P. Agrawal, J. Guo, P. Yu, C. Hbert, D. Passerone, R. Erni, and M. D. Rossell. Strain-driven oxygen deficiency in multiferroic $\{\mathrm{SrMnO}\}_3$ thin films. *Physical Review B*, 94(10):104101, September 2016.
- [77] Kota Tomita, Tomohiro Miyata, Weine Olovsson, and Teruyasu Mizoguchi. Strong excitonic interactions in the oxygen K-edge of perovskite oxides. *Ultramicroscopy*, 178:105–111, July 2017.
- [78] Nicholas L. McDougall, Rebecca J. Nicholls, Jim G. Partridge, and Dougal G. McCulloch. The Near Edge Structure of Hexagonal Boron Nitride. *Microscopy and Microanalysis*, 20(4):1053–1059, August 2014.
- [79] Tomohiro Miyata and Teruyasu Mizoguchi. Fabrication of thin TEM sample of ionic liquid for high-resolution ELNES measurements. *Ultramicroscopy*, 178:81–87, July 2017.
- [80] Robert F. Klie, Haibin Su, Yimei Zhu, James W. Davenport, Juan-Carlos Idrobo, Nigel D. Browning, and Peter D. Nellist. Measuring the hole-state anisotropy in $\{\mathrm{MgB}\}_2$ by electron energy-loss spectroscopy. *Physical Review B*, 67(14):144508, April 2003.

- [81] Stefan Nufer, Thomas Gemming, Christian Elsässer, Sibylle Kstlmeier, and Manfred Rhle. Core-hole effect in the ELNES of α - Al_2O_3 : experiment and theory. *Ultramicroscopy*, 86(3):339–342, February 2001.
- [82] Shang-Peng Gao, Chris J. Pickard, Alexander Perlov, and Victor Milman. Core-level spectroscopy calculation and the plane wave pseudopotential method. *Journal of Physics: Condensed Matter*, 21(10):104203, 2009.
- [83] Kevin Jorissen. *The ab initio calculation of relativistic electron energy loss spectra*. PhD thesis, University of Antwerp, 2007.
- [84] W. Kohn and L. J. Sham. Self-Consistent Equations Including Exchange and Correlation Effects. *Physical Review*, 140(4A):A1133–A1138, 1965.
- [85] E. L. Shirley, J. A. Soininen, and J. J. Rehr. Modeling core-hole screening in core-excitation spectroscopies. *Physica Scripta*, 2005(T115):31, 2005.
- [86] Peter Rez and David A. Muller. The Theory and Interpretation of Electron Energy Loss Near-Edge Fine Structure. *Annual Review of Materials Research*, 38(1):535–558, 2008.
- [87] Shang-Peng Gao, Chris J. Pickard, Mike C. Payne, Jing Zhu, and Jun Yuan. Theory of core-hole effects in $L_{2,3}$ core-level spectroscopy of the first-row elements. *Physical Review B*, 77(11):115122, 2008.
- [88] J. Hubbard. Electron correlations in narrow energy bands. *Proc. R. Soc. Lond. A*, 276(1365):238–257, November 1963.